1 Second revision

2 **Large, sustained, vertical winds observed in the thermosphere during**

3 **transient cusp heating**

4 Anasuya L. Aruliah, University College London, Gower Street, London WC1E 6BT, UK.

5 Herbert C. Carlson, Space Weather Center, Center for Atmospheric and Space Sciences,

6 Utah State University, Logan, Utah, USA.

7 Amy Ronksley, University College London, Gower Street, London WC1E 6BT, UK.

8 Ian McWhirter, University College London, Gower Street, London WC1E 6BT, UK.

9 John W. Meriwether, Department of Physics and Astronomy, Clemson University, Clemson,

10 South Carolina, USA.

11 Timothy C. Spain, University College London, Gower Street, London WC1E 6BT, UK.

12 Ian McCrea, Space Science and Technology Department, CCLRC Rutherford Appleton

13 Laboratory, Chilton, Didcot, Oxfordshire, OX11 0QX, UK.

14 Adrian Grocott, Radio & Space Plasma Physics Group, Department of Physics & Astronomy,

15 University of Leicester

16

17 Corresponding author: Anasuya L. Aruliah, University College London, Gower Street, London

18 WC1E 6BT, UK (a.aruliah@ucl.ac.uk)

19 *Submitted to J.Geophys.Res.*

20

21 **Abstract**

22 We provide new optical and radar observations here to highlight conditions under which the

23 polar thermosphere varies more rapidly in space and time than is commonly anticipated.

24 This work represents an example of observations of localized thermospheric upwelling

25 winds at Svalbard on 22 January 2012, under cusp conditions that are commonly associated

26 with flux transfer (or geomagnetic reconnection) events. The upwelling winds observed by

27 the narrow field Fabry-Perot Interferometer (FPI) were unexpectedly large, and sustained

28 over tens of minutes. These are the first co-located and independent measurements of the

29 thermosphere (FPI) and ionosphere (EISCAT Svalbard Radar - ESR), supported by CUTLASS

30 radar observations of ion velocities. The coordinated FPI/ESR experiment was designed for

31 the specific purpose of testing predictions based upon a recently published frictional drag

32 heating mechanism. This was formulated to explain the cusp density enhancements (up to a

33 doubling of density) seen at CHAMP altitudes of around 400 km. The observations show

34 substantive agreement with the prediction that energy deposition by frictional drag heating

35 during transient cusp heating events, can be steered to high enough altitudes by soft

36 particle precipitation to result in the large upwelling observed.

37

38 1. **Introduction**

39

40 One of the frequently cited papers within the past decade for upper atmospheric research

41 has been the CHAMP satellite finding by *Lühr et al.* [2004] of a near doubling of the

42 thermospheric density over the geomagnetic cusp region. This was a localised and

43   persistent feature that covered a horizontal distance of only a few hundred kilometres. A

44   density bulge greater than 1.2 times the background level was seen in ~50% of the

45   observations when CHAMP crossed the cusp, and even more frequently with the GRACE

46   satellite at 480km altitude [*Kervalishvili and Lühr*, 2013]. The cusp thermospheric density

47   bulge was the subject of two special sessions at the 2011 CEDAR/GEM Santa Fe conference.

48   This one finding has represented a major challenge to modelers to determine and

49   reproduce the mechanism that can cause such a persistent meso-scale feature in the

50   thermosphere. The high viscosity of the thermosphere is expected to produce large

51   temporal and spatial scale sizes of hours and a few thousand kilometres, respectively, for

52   thermospheric structures. Thus, vertical wind variations are expected to be small and short-

53   lived. However, with the increasing sensitivity of detectors used with Fabry-Perot

54   Interferometers (FPIs) over the last 20 years, there have been observations of strong vertical

55   winds in the auroral regions that contradict this assumption [e.g. *Price et al.,* 1995, *Aruliah*

56   *et al.,* 1995], but they are infrequent since hydrostatic equilibrium generally prevails. FPI

57   observations are typically narrow fields-of-view, with cycles of look directions, so large

58   vertical winds appear as single measurements within one cycle. Our experiment used

59   multiple vertical look directions in order to follow the upwelling and verify that it was real

60   by the consistency of successive measurements. Now that we are aware that large vertical

61   winds occur, we expect to see more experiments optimised to look for them. Conventional

62   modeling procedures place ion frictional heating predominantly in the E-region.

63   Consequently they have required unrealistically large quantities of energy to drive the

64   required upwelling of thermospheric gas to match CHAMP's observations. Thus, *Demars and*

65   *Schunk's* [2007] simulation applied 110 times the typical measured values of ion-frictional

66   heating in the cusp. *Crowley et al.* [2010] was the only other paper that successfully

67   modeled the observed doubling of air density, using input parameters that matched the

68   observed data, confirming the need for more realistic data input versus the use of

69   climatological data. Other studies proposed different mechanisms for the upwelling and

70   produced more modest density increases. *Clemmons et al*. [2008] presented Streak satellite

71   observations that showed density depletions of the thermosphere at altitudes of 250 km,

72   well below the altitude of CHAMP. They suggested that their observations challenged the

73   premise of Joule heating as the source mechanism since typically Joule heating is dominant

74   below 200 km altitude and peaks around 150 km. Their model study indicated that soft

75   particle precipitation heating was sufficient to produce suitably large vertical winds of up to

76   30 ms^{-1} above altitudes of 300 km to account for the density enhancement seen by CHAMP.

77   *Sadler et al.* [2012] used particle measurements from the FAST satellite in a time-dependent

78   three-fluid numerical model to produce density enhancements of up to 1.04 times the

79   background neutral density enhancements near 400 km, with upwellings of 20 ms^{-1}. The

80   modeling study by *Zhang et al.* [2012] achieved density enhancements of 25% at 400km

81   altitude using the Coupled Magnetosphere-Ionosphere-Thermosphere (CMIT) model when

82   they switched on soft electron precipitation simulated using an empirical relationship

83   between enhancement of the electron flux and downward flowing Poynting flux.

84

85   Previously *Carlson et al*. [2012] proposed that energy deposited at a higher altitude, and

86   only briefly, is capable of producing a doubling of density from a realistic energy source (i.e.,

87   within the range of actual observations). In the dark cusp, the suggested higher altitude of

88   energy deposition would be the direct consequence of soft particle precipitation thereby

89   determining the altitude profile of Joule/frictional drag energy deposition rate. The altitude

90 profile augments energy injection from transient plasma flow jets, as detailed in that paper,

91 which is a necessary additional energy source to achieve the large density enhancements (>

92 20%) seen regularly by CHAMP. *Deng et al.* [2013] systematically introduced ions, electrons

93 and Poynting flux heating to drive their model, which does not assume hydrostatic

94 equilibrium. This was not found adequate (see their summary breakdown of heating in their

95 Table 1) and an additional quantity of Poynting flux was required in the cusp, with Pedersen

96 conductivity used to control the altitude distribution of Joule heating. The combination of

97 soft particle precipitation and Poynting flux produced > 50% increase in the cusp density

98 under equinox conditions, when the cusp is sunlit. However, in this paper we are dealing

99 with a case featuring a mid-winter dark cusp condition.

100

101 The Svalbard site passes under the cusp during the hours of darkness in December and

102 January, thus allowing independent, but co-located and simultaneous measurements of the

103 properties of the thermosphere and the ionosphere using two Fabry-Perot Interferometers

104 (FPIs) and the two EISCAT Svalbard Radars (ESR). An experiment was designed for the period

105 of the January new moon in 2012, when the cusp region was still dark, to measure the

106 critical parameters required to determine both the energy deposition in the cusp (by

107 thermal charged particles via frictional drag/Joule heating, plus consequences of energetic

108 charged particles) and the response of the thermosphere and ionosphere to this heat input.

109 The two ESRs were used to monitor the ionospheric variables of plasma density (Ne), ion

110 and electron temperatures (Ti, Te), and horizontal and geomagnetic field-aligned plasma ion

111 drifts (Vi, $V_{//}$). The vertical and horizontal components of the winds of the thermosphere, as

112 well as the temperature, were independently monitored using both a narrow field FPI and a

113   Scanning Doppler Imager (SCANDI), which is a wide-field FPI [*Aruliah et al.*, 2010]. The

114   measurements were designed to achieve definition of the time-dependent altitude profile

115   of Joule heating/frictional drag heating, plus particle heating by determining the *input*

116   energy deposition rate as measured by the ESR, while simultaneously observing/mapping

117   the overhead *response* from the 3D wind field using the FPI and SCANDI. The all-sky SCANDI

118   measurements provided regional context for the horizontal distributions of the winds,

119   neutral temperatures and auroral emission intensities thus revealing the response of the

120   thermosphere over a range of latitudes within the frame of the forcing heating function

121   imposed by the magnetosphere and ionosphere that was sweeping past overhead. This

122   input of observational data would be used as input specifications to drive existing models

123   realistically. It was intended that the observed wind field response would be compared with

124   that derived from both the first order analytic evaluation of the proposed mechanism plus

125   the results obtained by a detailed study of the time-dependent 3-D physics of a

126   computational model. The goal of these measurements was to test the *Carlson* [2012]

127   mechanism, either to prove it right and refine it, or to prove it wrong with sufficient

128   quantitative definition to be the basis for formulating a new mechanism.

129

130   This paper presents the optical and radar observations, which are the first near-common

131   volume observations of both substantive cusp frictional drag heating and soft-particle

132   precipitation combined with an event that featured large, sustained, thermospheric

133   upwelling. In an accompanying paper currently under preparation we will determine the

134   heating using the UCL Coupled Middle Atmosphere and Thermosphere model (CMAT2).

135   Since this first campaign observed thermospheric upwelling events larger than anticipated,

136   one can well ask are these data extreme or exceptional? The CME was unusual and it is to

137   this that we attribute the departure of the *Tn* from MSIS. However, the cusp test time was

138   hours later and its signatures were normal. The optical and radar observations within the

139   three hours in the cusp show all the characteristics and signatures of a typical geomagnetic

140   reconnection event. Nothing unusual or extreme was observed during the time in the cusp

141   in any signatures in *Te*, *Ti*, *Vi*, *Ne*, or 630.0 nm MSP intensities data. Furthermore, the Kp

142   values were quiet to moderately active (Kp = 1- 1+ 4+ 4-) during the period 00 - 12 UT on

143   22 Jan 2012. While the *Carlson et al.* [2012] model study chose a test case of 3000 ms^{-1} to

144   investigate whether a realistically extreme *Vi* could match the *Lühr et al.* [2004] density

145   extreme (which test it passed), the values of *Ti* encountered here indicated values of ($\underline{V_i}$ –

146    $\underline{V_n}$) below that extreme. It is suggested that the traditional assumption of quasi-static

147   hydrostatic equilibrium precludes models from generating vertical thermospheric winds

148   exceeding a few 10s of ms-^{1}. Yet we demonstrate here that, on the meso-scale, observations

149   show that large vertical winds exist at the same time as more moderate ($\underline{V_i}$ – $\underline{V_n}$) velocity

150   differences.

151

152   **2. Observations and Context**

153

154   University College London (UCL) operates both a narrow field-of-view (1˚) FPI and a wide

155   angle (134˚) SCANDI at the Kjell Henriksen Observatory (KHO, 78.15˚N, 16.04˚E) that is

156   managed by the University in Svalbard (UNIS). The KHO is a couple of kilometres from the

157   two EISCAT radars on a mountain on Svalbard. The FPIs are the workhorses of

158   thermospheric research, providing continual observations throughout the hours of

159   darkness, which, for Svalbard, means observations from late October to the end of March

160   every winter. Clear skies are required for useable measurements when there is no cloud

161   scatter.

162

163   The UCL FPI has a sensitive Electron Multiplying Charge Coupled Device detector (Andor

164   iXon 887) capable of measuring the red line 630 nm emission at exposure times of a few

165   tens of seconds. The SCANDI is a state-of-the-art all-sky FPI, and the instrumental details

166   are described by *Aruliah et al.* [2010]. The SCANDI has been running operationally since

167   January 2007 with 25 sectors. For this campaign we increased the SCANDI horizontal spatial

168   resolution to 61 separate sectors mapped onto the whole sky overhead using a cadence of 7

169   minutes. This gave a sufficient signal since solar activity has been increasing after several

170   years of solar minimum conditions. Both the narrow field FPI and all-sky SCANDI observed

171   the 630 nm emission of atomic oxygen, which typically has a peak emission height at ~240

172   km in the upper thermosphere [e.g. *Vlasov et al.*, 2005].

173

174   Figure 1a shows the spatial extent of the IMAGE magnetometer network, which covers the

175   whole of the auroral and polar cap region in the Scandinavian sector (courtesy IMAGE). The

176   red dots represent the locations of the magnetometers. The region of the IMAGE

177   magnetometer array observations (Figure 1b) provides a good coverage of the Scandinavian

178   auroral and polar cap areas, and these IMAGE results complement the data from many

179   other instruments located on Svalbard and mainland Scandinavia that are operated by

180   several international teams. Superposed on the map is a projection on the sky, at an altitude

181   of 240 km, of the 61 SCANDI sectors, aligned along the geomagnetic meridian, which is at

182   the azimuth of 328˚ (-32˚). Figure 1c shows the latitudinal/longitudinal distribution of the 61

183   SCANDI sectors as well as the sector locations of the narrow field FPI look directions and the

184   radar field-aligned look direction at 240 km altitude.

185

186   The single look direction of the narrow field FPI directly measured the vertical wind

187   component at high cadence, using 30 seconds integration to study the localised small-scale

188   response of the thermosphere. This observing strategy was interspersed with looks to the

189   geographic North East (NE) and South West (SW) every 15 minutes to provide context

190   regarding the horizontal wind behavior. The observing sequence was: a series of 11 Zenith

191   images, then Calibration lamp (neon, 630.2nm), then another series of 11 Zenith images,

192   ending with SW, NE, Calibration Lamp. The possible FPI look directions are physically limited

193   in this instrument to geographic N, NE, E, SE, S, SW, W and NW. Since geomagnetic north is

194   at azimuth -32˚ with respect to geographic north, the SW and NE look directions are the

195   nearest equivalent to the geomagnetic West and geomagnetic East directions, respectively.

196

197   The experiment design originally planned required that the smaller EISCAT radar 32m dish

198   scan from north to south along the line of meridian at the highest possible speed (2-4

199   minute cycle times have been achieved) to determine the plasma velocities from the line-of-

200   sight measurements obtained. This has been a standard procedure since 2000 [*Carlson et al*,

201   2006]. The assumption inherent to this strategy is that the plasma velocity does not change

202   much during the scan, so that the different look directions can be combined to determine

203   the velocity vector [e.g. *Etemadi et al.*, 1989], and flow shear boundaries can be tracked

204 with ~2-3 minute revisit time [*Carlson et al, 2006*]. The plasma velocity and density are

205 required to calculate the altitude profile of the frictional drag energy deposition rate.

206 Toward the end of the 2 week campaign, severe meteorological storm winds arose resulting

207 in the azimuthal drive failure of the 32m dish radar system, so the meridian radar scans

208 could not be continued. The radar was manually parked in a safe mode, which was the field-

209 aligned (near vertical) pointing direction to reduce its exposure to the winds. Fortunately, a

210 Stratospheric Warming experiment was running when the CME encountered the Earth's

211 bow shock boundary at 06:17 UT on 22nd January 2012, and ESR observations were already

212 underway. The subsequent operations utilized a field-aligned radar mode, which meant that

213 only the component of the plasma velocity that was parallel to the Earth's geomagnetic field

214 could be measured. These are the observations presented in this paper. The lack of beam-

215 swinging measurements required the use of the ion temperature T_i as a surrogate measure

216 for the plasma velocity V_i [equation 1, as used by *St Maurice and Hanson*, 1982; *Thayer and*

217 *Semeter*, 2004; and *Schunk and Nagy*, 2009]. Equation 1 represents the balance between

218 the energy exchange term and the frictional heating term, which is a good approximation

219 below 400km, as demonstrated by, for example, *St Maurice and Hanson* [1982].

220
$$T_i \cong T_n + \frac{m_n}{3k_B}(\underline{V_i} - \underline{V_n})^2 \qquad\qquad [1]$$

221 Where T_n and T_i are the neutral and ion temperatures; $\underline{V_n}$ and $\underline{V_i}$ are the neutral and ion drift

222 velocities; m_n is the neutral particle mass*;* and k_B is the Boltzmann constant. Although *Ti* is

223 less directly linked to the driving physics of the ion frictional drag energy deposition rate, it

224 is equally valid to measure the Joule heating input parameters by using equation (3) rather

225 than equation (2), reproduced below from *Carlson et al*. [2012].

226
$$\frac{\partial E_n}{\partial t} = \sum_i (n_i m_i v_{in})(\underline{V_i} - \underline{V_n})^2$$
[2]

227
$$\frac{\partial E_n}{\partial t} = \frac{3k_B}{m_n} \sum_i (n_i m_i v_{in})(T_i - T_n)$$
[3]

228   Where the left hand side of equations 2 and 3 is the rate of change of energy E_n with time t

229   for the neutral gas; n_i is the number density of the ions which have mass m_i; and v_{in} is the

230   ion-neutral collision frequency.

231

232   Figure 1b shows plots of the magnetometer *x*-component deflections from all available

233   IMAGE magnetometer sites on that night. These are stacked in order of latitude with the top

234   plot from the highest latitude magnetometer at Hornsund on Svalbard (HOR geographic

235   latitude 77.00°N, CGM latitude 74.13°N). The second highest latitude magnetometer data

236   available is quite far away at Kevo (KEV geographic latitude 69.76°N, CGM latitude 66.32°N).

237   The CME impact was seen as a sudden deflection at 06:12 UT, followed by geomagnetic

238   pulses with periods of about 200 seconds during the period 08-10 UT that were seen as far

239   south as Tartu in Estonia (58°N). These are identified by auroral region magnetometers as

240   Pc-5 ULF waves, and their presence is typical of the cusp aurora [e.g. *Anderson*, 1993].

241

242   Figure 2 shows a comparison of the profile of electron density versus distance along the

243   geomagnetic field direction observed by the 42 m ESR radar dish between 06-12 UT on the

244   22nd January 2012 (Fig 2a), with the high time resolution narrow field FPI measurements of

245   630 nm intensities (Fig 2b) and winds observed in the zenith direction (Fig 2c). It was very

246   quiet for several days before the 22nd January, and the Meridian Scanning Photometer data

247   (not shown here) showed the dayside auroral oval was very contracted until near 08:00 UT.

248   Two short pulses of electron precipitation were observed after the CME arrived, which are

249   marked in Fig 2a by the two red blobs beginning around 06:20 UT and 07:15 UT between

250   altitudes of 200-300 km. Note that at night, when there is no photoionisation, a standard

251   measure of on-going plasma production by precipitation is enhanced electron density below

252   ~200 km where high recombination rates remove ionization within seconds after the

253   cessation of production [*Robinson et al.*, 1987]. At greater heights, where charged particles

254   have longer lifetimes, very soft particle production can also increase the F region density

255   enhancements to ~ a few times 10^{11} m^{-3}; while near the F region, peak densities of the order

256   of 10^{12} m^{-3} are normally attributed to transport from regions of solar EUV production - a

257   phenomena common at Svalbard within a few hours either side of local magnetic noon (MLT

258   noon ~09 UT) for southward IMF conditions (e.g. *Crowley*, 1996; *Carlson* 2012. The second,

259   shorter-lived pulse of increased electron density in the *F*-region occurred between 07:15-

260   07:30 UT. There was then observed a sustained period of precipitation between 08:20-10:50

261   UT. The additional contribution from F region anti-sunward plasma transport produced high

262   electron densities above 200km when the electron density reached values of the order of

263   10^{12} m^{-3}, which was similar to ionization levels during the daytime. Examining only the

264   electron density enhancements below 200 km, a reliable indicator of direct particle

265   production in the dark cusp [*Wickwar et al*, 1975; *del Pozo et al*., 1997], we see hard particle

266   precipitation ending near 08:05 UT, two bursts of soft particle precipitation (as just noted),

267   and thereafter recurring soft but not hard particle precipitation. This was recognisable as

268   soft particle precipitation typical of the cusp region that passes over Svalbard usually

269   between 08-12 UT, but uncommonly intense and recurring. During the latter period while

270   the electron densities can be seen to have disappeared in the E-region, the enhanced

271 electron densities near the D and E regions before 08:00 UT can lead to what is commonly

272 known as "radio blackout", which we note in passing is a Space Weather problem for HF

273 communications.

274

275 A comparison of Figures 2a and 2b shows that there was a close correspondence between

276 electron density enhancements as observed by the ESR and peaks in the 630 nm intensities

277 as observed by the narrow field FPI owing to the sum of impact excitation and dissociative

278 recombination of the molecular oxygen ion, which is the dominant excitation mechanism for

279 atomic oxygen at night in the absence of electron impact excitation [e.g., *Vlasov et al.*,

280 2005]. Before the CME encountered the Earth, the 630 nm intensities were very low at a

281 few hundred data counts, and afterwards, at 06:17 UT, the 630 nm intensity instantly rose

282 to between 1000-2000 data counts. The FPI intensities are not calibrated so the data counts

283 are in arbitrary units. Comparison with the University Centre in Svalbard (UNIS) Meridian

284 Scanning Photometer at Longyearbyen indicates that for the narrow field FPI data one data

285 count corresponds to about 1 Rayleigh.

286

287 Figure 2c shows the three directions (vertical component plus horizontal components for NE

288 and SW directions) of the narrow field FPI thermospheric wind speed, calculated from the

289 Doppler shifts of the 630 nm emission from the three look directions. The size of the wind

290 error is directly related to the 630 nm intensity, and consequently, this error is typically anti-

291 correlated with the electron densities (excepting other 630 nm excitation processes). The

292 zenith winds between 00-06 UT were seen to hover around zero, with large errors, ~±25-35

293 ms^{-1}, due to the low 630 nm emission intensity. The procedure of determining the zero

294   Doppler shift baseline is critical for calculating the small vertical winds, where the errors are

295   of a similar order of magnitude. Details may be found in *Aruliah and Rees* [1995], but

296   basically it was assumed that over the six hour period between 00-06 UT, when there was

297   no, or very weak auroral activity (as indicated by the IMAGE magnetometer plot in Figure

298   1b), the values of the vertical wind averaged to zero. The average offset (calculated as the

299   six hour average of the difference between the zenith and the calibration lamp data) was

300   added to the calibration lamp data and then used to maintain this zero Doppler shift

301   reference for the remainder of the night series of observations.

302

303   As the CME encountered the Earth's magnetosphere, the intensity rose, decreasing the

304   errors, but the zenith winds were still small, though systematically upward, with an average

305   value of 12 ms^{-1} between 06:00-08:00 UT. This finding is discussed further below with

306   reference to Figure 6. Only when strong cusp precipitation was seen by the field-aligned ESR

307   between 08:30-10:50 UT (Figure 2a), in concert with frictional drag heating as indicated by

308   the ion temperatures (discussed later with reference to Figure 6), did the vertical winds

309   increase sharply to a maximum of 199 (±9 error) ms^{-1} at 08:48 UT but averaging to a

310   systematic upwelling of +51 ms^{-1} over a 4 hour period between 08:00-12:00 UT. The

311   fluctuation during this period due to upwelling and downwelling had a standard deviation of

312   ± 44 ms^{-1} about the systematic upwelling. After the precipitation a shorter period of

313   downwelling was observed between 11:00-12:00 UT, reaching a maximum downward speed

314   of -49 (±14 error) ms^{-1} at 11:20 UT. These are unprecedented observations of high,

315   sustained vertical winds seen at high time resolution, simultaneously (and independently)

316   alongside radar observations of cusp precipitation.

317   The winds in the geomagnetic zonal direction (as represented by the narrow field FPI look

318   directions to the geographic NE and SW) were relatively small before the CME arrived,

319   reaching a maximum of 200 ms^{-1} westwards just after 01 UT. The volumes that the narrow

320   field FPI sees when looking to the geomagnetic East and West at an elevation angle of 30°

321   and an emission altitude of 240 km, are separated by a horizontal distance of 830 km. The

322   zonal wind components measured to the east and west before 06:17 UT were similar and

323   the mean zonal flow across the FPI field of view was westward. However, as soon as the

324   CME arrived, the zonal winds seen to the geomagnetic East accelerated to nearly 342 ms^{-1}

325   westwards by 07:15 UT, and then swung eastward to 208 ms^{-1} by 10:00 UT before swinging

326   back westward by 11:00 UT. The geomagnetic zonal winds seen to the west were different,

327   and remained westward for the whole period after the CME arrived, just showing a trend to

328   become increasingly westward, reaching a peak value of 411 ms^{-1} westwards by 12:00 UT.

329   From 08:50-12:00 UT there was a very strong gradient in the zonal wind component.

330

331   In order to have as high a time resolution as possible in the vertical direction, the narrow

332   field FPI was set only intermittently to observe as close as possible to the geomagnetic East

333   and West (i.e. the narrow field FPI fixed look directions to the geographic NE and SW). No

334   geomagnetic meridional observations were made. Through ion-neutral coupling, the zonal

335   winds will reflect the IMF B_y magnetic tension force on the ionospheric flow jets during

336   geomagnetic reconnection. The SCANDI observations provided a large-scale context for the

337   cusp activity. Figure 3 shows the SCANDI data between 05:42-11:57 UT. The SCANDI field-of-

338   view has a diameter of ~1130 km (equivalent to ~10° latitude), divided into 61 sectors. The

339   figure is drawn so that the top of each SCANDI circle points to geomagnetic North (azimuth

340   = -32°) as shown in greater resolution in Figure 1. The FPI's NE and SW look directions map

341   onto the boundaries between zones 40 and 58 for the FPI NE look direction, and between

342   zones 31 and 49 for the FPI SW look direction.

343

344   The SCANDI field-of-view is large enough to image most of the thermospheric upwelling

345   bulge with excellent spatial and temporal resolution. This instrument, an all-sky FPI, has only

346   recently been introduced to thermospheric research, and there are currently only four other

347   Scanning Doppler Imagers in operation (in Alaska at Poker Flat, Gakona and Toolik Lake, and

348   in Antarctica Mawson), all built by Dr Mark Conde at the University of Alaska, who

349   pioneered the technique [e.g. *Conde et al,* 2001]. However, only the UCL SCANDI is at a

350   latitude that can observe the cusp under suitable geomagnetic conditions. The evolution of

351   the thermosphere (at an altitude of around 240 km) over the period 05:42 - 08:52 UT can be

352   seen from the line-of-sight wind components (top row) and thermospheric temperature

353   (middle row), which shows a clear difference of values between before and after the CME

354   reached the Earth. Prior to this time the 630 nm intensities were low, and immediately

355   afterwards, a clear geomagnetic north-south division appears that shows the 630-nm

356   intensities to be at least three times higher to the geomagnetic north until 08:30 UT. The

357   630 nm emission intensities (bottom row) formed a band that moved equatorwards until it

358   was overhead by 08:52 UT, remaining overhead until 10:51 UT, and then later moving into

359   the southern half of the SCANDI field-of-view. The narrow field FPI saw large vertical winds

360   while the aurora was overhead.

361

362   The results presenting neutral temperatures are interesting (middle rows of Fig 3). Before

363   the CME arrived, there was a significant gradient so that it was warmer to the south by a

364   few hundred Kelvin. As soon as the CME encountered Earth, the neutral temperature over

365   the whole of the SCANDI field-of-view dropped to around 700-800K. This occurred because

366   there was some E-region precipitation between 06:17-07:15 UT as shown by the ESR

367   electron densities. Consequently, it is possible that the 630-nm peak emission height

368   dropped below the usual 240 km causing the narrow field FPI to sample a lower height

369   region during this period. Since our focus is on thermospheric upwelling, the height of the

370   630 nm emission layer has not been considered further. This is because above

371   ~250 km the high viscosity of the thermosphere makes the height profile of

372   neutral temperature isothermal, and the winds become uniform, consequently the altitude

373   sampled is not critical. Although there is a steep vertical gradient in neutral winds and

374   neutral temperature below 200 km, the quenching of the red line emission by molecular

375   oxygen and nitrogen means that there is no 630nm emission below 200 km altitude (e.g.

376   Vlasov et al., 2005). This gives a lower limit to the altitude sampled by the FPIs. Downwelling

377   and prolonged E-region precipitation would require a closer study regarding the question of

378   what height was being sampled by the FPI, but this issue is not the focus of this paper. After

379   07:18 UT the neutral temperatures were more typical of the upper thermosphere. Although

380   there was another brief burst of E-region precipitation between 07:30-07:45 UT, it was too

381   short-lived and the neutral temperatures did not fall as before.

382   Figure 4a shows the neutral temperatures observed in the vertical look direction at high

383   time resolution by the narrow field FPI (green line in graph). This was compared with the

384   lower resolution observations in the NE and SW direction, and also cross-compared with the

385 SCANDI central zone observations (black, red and blue lines, respectively). The all-sky

386 SCANDI and narrow field FPI temperatures were consistent, although the SCANDI

387 temperatures were noisier during the low 630 nm intensity period before 06:17 UT. The NE

388 and SW FPI observations corroborated the significant temperature gradients seen in high

389 spatial resolution across the SCANDI field-of-view. The MSIS neutral temperatures are

390 shown in Figure 4b for comparison, where the temperatures for the volumes corresponding

391 to the 3 narrow field FPI look directions are plotted independently. The series of MSIS

392 models [*Hedin*, 1992] and later version NRLMSISE-00 [*Picone et al*., 2002] are driven by the

393 geomagnetic and solar flux indices: Kp and $F_{10.7}$, respectively, for the given date. Since we

394 were interested only in the thermosphere above 120km, the MSIS90 version was used.

395 The MSIS90 temperature between 05-06UT was a good match with the FPI/SCANDI

396 measurements. Subsequent to the CME, the FPI/SCANDI observations showed

397 thermospheric temperatures steadily increasing from ~850 to 1200K, while the MSIS model

398 showed an immediate increase of over 200 K to 1060 K at 06 UT, followed by a stepping

399 down of temperature to just below 1000 K at 12 UT. This poor representation of the neutral

400 temperature by MSIS was due largely to the Kp index, which is derived from the maximum

401 geomagnetic deflection during a 3 hour interval, and consequently results in a crude

402 measure of thermospheric response. Not only was the temperature trend different, with a

403 smaller dynamic range, but there was very little latitudinal spread in the MSIS temperatures

404 compared with the FPI/SCANDI observations. The almost negligible temperature gradient in

405 MSIS decreased between 06-12 UT, unlike the increase seen in the FPI/SCANDI

406 observations. MSIS is a commonly used semi-empirical model of the neutral atmosphere,

407   but its limitations for modeling the dynamic auroral region, though known by the

408   community, are usefully illustrated by this comparison.

409

410   Figure 5 shows SCANDI horizontal neutral wind vectors in geomagnetic coordinates

411   (geomagnetic North is at top of each circle, and geomagnetic East to the right) as observed

412   around the period of upwelling 05:50-11:57 UT when the site passed under the cusp. The

413   blue line indicates the anti-sunward direction that nominally is the direction of pressure

414   gradient driven flow, over the pole from the hot dayside toward the cold nightside. The red

415   line shows the geographic NE-SW line-of-sight direction, for comparison with the narrow

416   field FPI look directions. The vectors were determined from the line-of-sight measurements

417   for each ring using the method described in *Conde and Smith* [1998]. The SCANDI winds

418   began to pick up speed about 30-40 minutes after the CME developing a north-south

419   division of structure in the wind field over the SCANDI 1130 km diameter field-of-view that

420   corresponded to a sharp intensity gradient seen in the red (third) rows of Figure 5 between

421   06:19 - 08:08 UT. The wind direction within the SCANDI field-of-view seemed to rearrange

422   itself during this period. As the auroral activity passed overhead of SCANDI the wind field

423   became more uniform. Over a period of 3.5 hours a swing in the general wind vector

424   direction occurred, changing from a geomagnetic northwest (beginning to turn at about

425   09:14 UT), to geomagnetic northeast (by 09:29 UT), and back to northwest wind flow (by

426   10:51 UT). The all-sky SCANDI vectors were consistent with the narrow field FPI line-of-sight

427   observations (Figure 2c), which indicated a considerable gradient in the geomagnetic zonal

428   winds between 09-11 UT. Note that the SCANDI observations were integrated over a period

429   of about 7 minutes while the FPI observations were all 30-second exposures. Figure 5

430   indicates how quickly the thermospheric wind responds to the cusp ion frictional drag

431   energy injection and particle precipitation as it passed overhead.

432

433   Figure 6 focusses in on the period 06-09UT. Electron densities between 100-210 km altitude

434   (Figure 6a) are combined with a plot of the vertical wind variation, *Vn* (Figure 6b) and a

435   color-shade plot for *Ti* (Figure 6c). Before 09:00 UT there was a simple situation of clearly

436   individual flux transfer events (FTEs). Data after 09:00 UT have not been shown because the

437   large number of FTEs resulted in overlapping signatures which complicated any

438   interpretation. Figure 6b shows a small systematic upwelling of 12 ms^{-1} (173 consecutive

439   data points with time resolution of 32 seconds, which allows for computer processing time;

440   and excluding the intermittent NE, SW and calibration lamp measurements) sustained

441   throughout the period 06:00-08:00 UT. Figure 6b shows that for most of the time between

442   06:00 – 08:00 UT the ESR observed a strong largely persistent E region produced by more

443   energetic particles (evidenced by production between ~100-150 km). In addition there were

444   intermittent weak soft particle fluxes (additional production above ~170 km) and an

445   intermittent F region of electron density so low that ion production by these soft particle

446   fluxes can be expected to have contributed materially to its net electron content. These F1

447   region *Ne* and conductivities produced by soft particles were quite similar to the *Ne* near

448   200 km during the upwelling events after 08:20 UT, but there were no high Ti values to

449   indicate high *Vi* flow jets. Therefore, as predicted by the *Carlson et al*, [2012] mechanism,

450   there cannot have been any strong F region response to Joule/frictional drag heating, which

451   accounts for the weak upwelling observed by the FPI. Recall that during this 06:00 – 08:00

452   UT time interval the auroral oval was contracted, and these soft particle fluxes were not

453   associated with near-cusp reconnection events. Thus, for these lower geomagnetic latitudes

454   overhead the ESR and FPI during 06:00 – 08:00 UT, there was no reason to anticipate any

455   large horizontal plasma flow velocities, although CUTLASS radar line-of-sight observations

456   indicated the presence of weak transients (shown in Figure 8). This is consistent with

457   observations of *Ti* less than 1500 K during this period, as shown in Figure 6. Note that,

458   assuming a linear response, $(\underline{V_i} - \underline{V_n})$ = 1000 ms^{-1} would correspond to ~10 % density

459   enhancement compared with a 3000 ms^{-1} shear to achieve a doubling of density as modeled

460   by *Carlson et al.* [2012]. Thus, although the E region had sufficient plasma density ready to

461   respond to energy deposition in the lower F region, *Ti* indicates that no significant frictional-

462   drag/Joule heating was taking place, and therefore $(\underline{V_i} - \underline{V_n})$ was small. For the particle fluxes

463   penetrating to E region heights, under these conditions, the literature [e.g. *Burns et al*,

464   1991] would indicate exceedingly modest heating effects. However, the sensitivity and high

465   time resolution of the narrow field FPI here allowed a search for a vertical wind response

466   previously too small to consider looking for. We note that the statistical error bars given do

467   not address possible systematic errors. Yet, given exhaustive work to remove such, and the

468   high frequency of calibration images built into the observing cycle, we interpret the small

469   but persistent upflow during these two hours as the first ever detection of this effect,

470   indicative of a net upflow created by the sum of energy input and E-region electrodynamics

471   below. Figure 6 compares this small largely persistent upwelling wind with the electron

472   density between 80-210 km. The small upwelling was seen immediately on the appearance

473   of energetic particle flux into the E region, but no obvious neutral response to enhanced flux

474   in the lower F region. This is consistent with our prediction. Soft particle precipitation

475   would favour heating and upwelling if large horizontal ion flow velocities were present, but

476   they are neither seen nor expected this far equatorward of the cusp before 08:00 UT. After

477   ~08:00 UT observations of upwelling are consistent with cusp behaviour after it moved to

478   the zenith region above the ESR and narrow field FPI instruments.

479

480   Additional support for the study comes from the Cooperative UK Twin-Located Auroral

481   Sounding System (CUTLASS) [*Milan et al*., 1997] radars. These provide observations of the

482   large scale horizontal plasma flow. There are two CUTLASS radars: at Hankasalmi, Finland

483   (62.3°N, 26.6°E) and Pykkvibær, Iceland (63.8°N, 20.5°W), which in their standard mode of

484   operation scan through 16 beams of azimuthal separation 3.24°, with a total scan time of 2

485   min. Each beam is divided into 75 range gates of length 45 km, thus forming 1200 "cells" in

486   which observations can be made. Radar signals, scattered from ionospheric magnetic field-

487   aligned irregularities in the E and F region, are Doppler shifted according to the motion of

488   the plasma in the radar's line-of-sight direction. In cases where the signal is orthogonal to

489   the magnetic field, it is backscattered to the radar and a measurement is obtained. No

490   backscatter is observed where no irregularities exist, or where the orthogonality condition is

491   not met, and as a consequence velocity measurements are not ubiquitous within the radar

492   field-of-view. This is illustrated by the plots in Figure 8 which show eight Hankasalmi radar

493   scans between 08:25 – 08:42 UT. A colour scale indicates the line-of-sight speed ranging

494   from -800 to + 800 ms^{-1}, where positive is towards the radar. The grey circle indicates the

495   500km boundary around Svalbard, which roughly corresponds to the range of the field-of-

496   view of the narrow field FPI. The first two plots of Figure 7 (08:26-08:27 UT) show the

497   Hankasalmi line-of-sight speeds just as the activity is appearing overhead of Svalbard. The

498   next six plots show Hankasalmi radar scans between 08:36 – 08:41 UT, which was a period

499   when large upwelling of the neutral gas was observed by the narrow field FPI. These high

500   time resolution consecutive plots illustrate the localised and transient nature of the large-

501   scale plasma flows, and also examples of the large plasma velocities observed here by

502   CUTLASS. Typically the appearance of reconnection transients have been observed by the

503   ESR to last ~19 minutes on average [Rinne et al., 2007]. Figure 8 shows an example of large

504   values of line-of-sight observations of $Vi > 800$ ms^{-1} to the north-east of Svalbard from the

505   Hankasalmi radar (left plot) and $Vi > -800$ ms^{-1} to the south-west from Pykkvibær (right plot)

506   yet there was no upwelling observed by the FPI. Since Ti overhead of the ESR was <1500 K

507   (equivalently $Vi - Vn < 1000$ ms^{-1}), upwelling should not be expected in the coincident FPI

508   field of view. Furthermore, the oppositely directed line of sight velocities with magnitudes >

509   800 ms^{-1} seen by CUTLASS were separated spatially by 2 hours MLT and thus could have

510   corresponded to different parts of the cusp plasma flow field, rather than a line of shear

511   flow passing through the field-aligned ESR beam. Consistent with this, no soft particle

512   precipitation was observed by the ESR.

513

514   The sustained and large vertical winds observed were unexpected. It was considered

515   whether auroral spectral contamination by the 10-7 band of the First Positive emission of N_2

516   could be responsible for the apparent appearance of extreme vertical winds as this band

517   overlaps the spectral region of the 630 nm emission [*Dieke and Heath*, 1959]. The narrow

518   field FPI and SCANDI filters are 1 nm in width, which potentially could allow the transmission

519   of one of the many branches of the neutral line N_2 first positive band (IPG 10,7) at 630.03

520   nm. Also considered (private communication, Don Hampton, Univ. of Alaska) was the

521   possibility of "hot oxygen" contamination in which a portion of the neutral atom population

522   represented by the 630 nm OI Doppler broadening spectral profile was accelerated by the

523   production of fast [O] atoms by charge transfer of an electron from fast oxygen ions in the

524   reaction of O^+(fast) + O(slow) => O^+(slow) + O(fast). The derived Doppler line center position

525   would then not be representative of the bulk neutral flow within the field-of-view of the FPI.

526   So we looked at the ESR measurements of the field-aligned plasma velocity. The spatial

527   separation at F-region altitudes of the ESR field-aligned beam and the vertical look direction

528   of the narrow field FPI was small compared to flow-jet channel-widths that are typically 1-2

529   degrees of latitude. In the time required for frictional drag heating to bring ions near the

530   values of the high ion temperatures observed, they will have moved only ~100 km in a flow

531   direction whose time duration will carry them between 1000-2000 km downstream along a

532   nominal L-shell aligned direction. Consequently we have considered the field-aligned ESR

533   and vertical FPI measurements to be collocated for any practical purpose, allowing us to

534   make direct comparisons. The ESR field-aligned velocity measurements showed an ion

535   upflow speed of over 200 ms^{-1} for altitudes only above 400 km. At these altitudes the O^+

536   population that might be responsible for "hot oxygen" contamination through charge

537   exchange is typically 4-6 orders of magnitude smaller than the neutral oxygen population at

538   the 630nm emission peak altitude of 240 km. As another possible upper limit, *Shematovich*

539   *et al.* [1994] have found hot oxygen to be 1% of the cold oxygen density above 300 km. The

540   full width half maximum of the 630nm emission height profile is ± 50 km [e.g., *Vlasov et al.*,

541   2005), so possibly ~10% of the emission comes from altitudes > 300 km, of which 1% might

542   be hot oxygen. We therefore do not yet find evidence to support the idea of fast O

543   contamination as the reason for the large vertical winds. A modelling study of the 630nm

544   emission height profile is required, which is outside the scope of this paper.

545

3. Discussion

Carlson et al [2012] used the UCL Coupled Middle Atmosphere and Thermosphere [CMAT2, Harris et al., 2002] model to show that it was possible, by simply using realistic electron density height profiles and plasma-neutral velocity differences (V_i - V_n), to produce a realistic heating source capable of producing a doubling of the thermospheric density at the CHAMP altitude. CMAT2 is a time-dependent 3-dimensional global circulation model, which solves the equations of continuity, momentum and energy. The model simulated a typical plasma flow channel using a Gaussian profile to represent heating using a standard deviation of 4° geomagnetic latitude (i.e. 2 grid points), with a typical energy deposition represented by a linear increase from zero to a maximum value over 10 minutes, followed by a linear reduction to zero over the next 10 minutes [Carlson et al, 2006]. The heating profile was not explicitly calculated in terms of frictional velocity difference (V_i - V_n), but was designed to be representative of Joule heating at the high end of the typical range, which is 1-3 kms^{-1}. The aim was to replicate the near doubling of density reported by Lühr et al. [2004], which would have represented an extreme response of the thermosphere. A statistical analysis of the cusp region densities for CHAMP orbits showed the average density enhancement was 1.33 times the background [Kervalishvili and H. Lühr, 2013] .

To put the choice of plasma velocity in context, Figure 9 shows the frequency of observation statistics of the line-of-sight ion velocities measured by both of the CUTLASS radars during the period January-December and 07-11 UT (i.e. Svalbard dark cusp) between the years 1998-2009. The data are divided into solar maximum years (1998-2003) in the left hand column, and solar minimum (2005-2009) on the right. The top row shows the Hankasalmi

569 line-of-sight histograms, and the second row the Pykkvibær histograms. Since positive is

570 defined here as positive velocity towards the radar, for this dataset, positive velocities in the

571 Hankasalmi histograms represent the horizontal ion velocity components to the geographic

572 south (V_S) and in the Pykkvibær histograms to the geographic west (V_W).

573

574 The third row histograms zoom in on the magnitude of the line-of-sight velocities (blue =

575 Hankasalmi, red = Pykkvibær) to focus on the range 1000-3000 ms^{-1} and show how the

576 occurrence of V_i > 2000 ms^{-1} drops off rapidly. In addition, it is apparent that the occurrence

577 is generally lower for solar minimum. This solar cycle dependence is due to an associated

578 dependence on geomagnetic activity; in general increased activity provides a mechanism for

579 the generation of ionospheric irregularities. On shorter timescales, however, intense

580 activity (such as magnetospheric substorms, for example) can disturb the ionosphere and

581 result in absorption of the radar signal thus reducing the scatter occurrence [*Milan et al.*,

582 1999]. In addition, the scatter occurrence is sensitive to season and local time; however,

583 these factors were kept constant between our two solar cycle phases and so should not

584 impact our comparison of the two over such long timescales. Another factor to consider is

585 that the growth rate of the $\underline{E}$ x $\underline{B}$ instability that gives rise to the scattering irregularities is

586 dependent on the velocity of the bulk ion drift relative to the neutral background. If the

587 neutral wind velocity increased to equal the bulk ion drift, the growth rate of the

588 irregularities is expected to drop [*Milan et al.*, 1999]. Although the response time of the

589 neutral atmosphere to ion drag is expected to be slow (2-3 hours at nighttime for a large-

590 scale behaviour), it might be expected that the scatter occurrence would decrease if several

591 hours of constant applied electric field was experienced, or if there was rapid small-scale

592 thermospheric response.

593

594   The velocities themselves exhibit a general bias towards northward flows: the CUTLASS

595   histograms show the occurrence of northward flows inferred from the Hankasalmi radar are

596   ~75% of the total. The occurrence of westward flows inferred from the Pykkvibær radar is

597   similar to the eastward flows. Given the local time and latitude of the observations, one

598   might expect a preponderance of anti-sunward (northward) $\underline{E}$ x $\underline{B}$ convection to be

599   observed, corresponding to cusp flows into the polar cap.

600

601   Lastly, a number of additional features are apparent in the data. The peak at zero velocity

602   may be due to contamination from "ground" backscatter, where the radar signal has

603   refracted sufficiently to be transmitted down to the ground (from which it unsurprisingly

604   experiences little Doppler shift), before scattering back to the radar. In fact, ground scatter

605   is very common, however, much of this is removed via an automated process (see *Milan et*

606   *al*, [1997] for a detailed description of radar scatter types). Nevertheless, it is difficult to

607   ensure 100% removal via manual inspection of such a large data volume. The secondary

608   peak, in the Pykkvibær histograms (2nd row) at 350 - 400 ms^{-1}, is likely to be due to "Type I"

609   E-region scatter, which is constrained to be near the ion acoustic speed and is caused by

610   differential flow between ions and electrons; the so-called two-stream (or Farley-Buneman)

611   instability [*Farley*, 1963; *Buneman*, 1963]. The peaks at +/- 700 ms^{-1} evident in the data for

612   solar minimum would appear to correspond to "super-ion-acoustic echoes", as discussed by

613   *Milan et al.* [2003]. This latter paper shows that the occurrence of these echoes exhibits a

614   dependence on the line-of-sight angle, peaking at near 45° to the direction of the electrojet

615   flow. It also exhibits a radar frequency dependence, peaking at frequencies between 10 and

616   12 MHz. These findings argue against such echoes arising as a result of a heating-induced

617 elevation in ion-acoustic speed, and the question of their origin remains open. The peaks in

618 the Hankasalmi data at ~1500 ms^{-1} and ~1900 ms^{-1} are possibly attributable to an elevated

619 convection electric field during a single period of observation considering the low

620 occurrence.

621

622 Observations from the ESR or DMSP *Vi* measurements indicate that plasma shears of the

623 order of 3000 ms^{-1} are about the largest seen. Thus the mechanism tested by *Carlson et al*.

624 [2012] was modeled for a 3000 ms^{-1} shear, to investigate whether this maximum realistic

625 shear reproduced the maximum observed density enhancement reported by *Lühr et al*

626 [2004]. The histograms in Figure 9 indicate that there was a small (~1%), but not

627 insignificant, probability of *Vi* > 1500 ms^{-1} (which would create > 20% density enhancement).

628 It should be noted that the strict conditions required for HF backscatter may mean that the

629 CUTLASS histogram is not truly representative of the occurrence of very high values of *Vi*,

630 especially on the meso-scale spatial resolution of the CUTLASS range gates as represented

631 by pixel size. Furthermore, comparison of SuperDARN HF radars and DMSP satellite cross-

632 track ion drift measurements of *Vi* by *Drayton et al.* [2005] and comparison of CUTLASS HF

633 and EISCAT UHF measurements by *Davies et al.* [1999] both indicate that the HF radar

634 measurements are about 70% of the satellite and UHF incoherent scatter radar

635 measurements owing to differences in measuring temporal and spatial variations. The

636 strength of the SuperDARN network of coherent scatter radars is to provide large-scale

637 plasma flow structures at the F-region altitude, while the incoherent scatter radars provide

638 the fine detail and a height profile.

639

640   *Carlson et al.* [2012] aimed at modeling the maximum observed density increase.

641   *Kervalishvili and Lühr* [2013] show an average cusp density enhancement of ~1.33 with a

642   standard deviation of ~0.3 for local winter (their Figure 10). Statistically this means that

643   68.2% of observations show cusp density enhancement between 1.03-1.63 times greater

644   than the background. This raises an interesting question about the relation with the ion

645   velocity distribution: – could ion velocities of only a few hundred ms^{-1} be sufficient for cusp

646   upwelling? Yet the CUTLASS histograms indicate that the occurrence of line-of-sight Vi > 500

647   ms^{-1} is only 18%. Detailed comparisons with CUTLASS would require a separate study, which

648   is included in our future plans. But we should also consider the contribution of the neutral

649   winds to frictional heating. The SCANDI wind vector observations (Figure 5) indicated times

650   when the horizontal neutral wind speeds were up to 600 ms^{-1}, and consequently ($\underline{V}_i$ - $\underline{V}_n$) >

651   3000 ms^{-1} are plausible with smaller values of Vi.

652

653   The effect on the thermosphere was demonstrated in Figure 2a of *Carlson et al* [2012],

654   which shows a latitude-altitude plot of the thermospheric temperature enhancement, with

655   wind vectors superimposed. Their Figure 2b shows the ratio of thermospheric density

656   against a steady background state reached a peak value of 2.1, which was consistent with

657   CHAMP observations *Lühr et al*. [2004]. For model comparisons, vertical winds of a few tens

658   of ms^{-1} or greater cannot be modeled by Global Circulation Models that use the quasi-static

659   formulation of hydrostatic equilibrium as a constraint. This assumes an incompressible gas

660   in order to suppress spurious computational waves, but consequently loses the ability to

661   model vertical convection, i.e. large vertical winds, driven by true compressibility on smaller

662   spatial scales [e.g., *Eliassen*, 1949]. This assumption limited the speed of the upwelling

663   column modeled by CMAT2, but the final output density/temperature changes obtained

664 after integration over the space/time/path-length involved were realistic. The CMAT2

665 vertical winds were consistent with those reported by, for example, *Clemmons et al*. [2008]

666 and *Sadler et al* [2012] who considered only soft particle precipitation. In contrast, *Deng et*

667 *al.* [2013] were able to model 100 ms^{-1} upwelling using their (currently one of only two

668 unique to our field) non-hydrostatic equilibrium model driven by both soft precipitation and

669 Poynting flux, which is consistent with the FPI observations reported here.

670

671 Another important issue is the realism of total energy requirements. Traditionally the bulk

672 of frictional heating is delivered below 160 km which means lifting the entire atmospheric

673 column above the heating region, which demands unrealistically large energy inputs, as

674 demonstrated by *Demars and Schunk* [2008]. *Carlson et al* [2012] demonstrated that

675 entirely realistic energy inputs can readily achieve dramatic upper thermospheric density

676 and wind perturbations under conditions where energy was deposited only above ~160-180

677 km, or for short durations of a fraction of an hour. They further pointed out that large

678 plasma velocity shears, and the presence of soft particle fluxes in darkness (as here) create

679 such conditions. While particle heating (kinetic energy) can be deposited at any height

680 reached by the particles, the intense heating requires high-speed plasma flow jets (~2-3

681 kms^{-1}) [Figure 11 of *Carlson,* 2012]. This is confirmed by *Deng et al.* [2013] who have broken

682 down the energy contributions to cusp upwelling by particle precipitation and Poynting flux.

683 They corroborate other model simulations that show that soft particle precipitation

684 produces only weak density enhancements [e.g. *Clemmons et al.*, 2008, *Zhang et al.*, 2012].

685 The key role of the altitude of energy deposition has also been quantified in *Carlson et al*.

686 [2012]. Flow-jets deposit Joule heating energy only above 130 km where the Pedersen

687   conductivity dominates. Below this altitude ion-neutral collision frequencies exceed ion

688   gyro-frequencies, so that ions move with the neutrals and Hall currents dominate over the

689   Pedersen. More importantly, considerations regarding heat capacity and density make it

690   vastly harder and slower to heat the thermosphere between 120-150 km as compared with

691   160-200 km.

692

693   Thus, theory, experiment, and modeling agree that nightside auroral energy injection in the

694   E region finds a thermosphere too dense to respond significantly for any time scale that is

695   less than one hour [e.g. *Burns et al*., 1991]. Heating deposited at too high an altitude is less

696   effective because it loses the compounding amplification of many scale heights of upwelling

697   to help double the density by the time the gas reaches 400 km. For these and further

698   reasons summarized in *Carlson et al.* [2012], heating in the altitude region 160-200 km may

699   be regarded as the most effective region for creating density bulges by upwelling. Thus we

700   will focus here on correlating observed strong thermospheric upwelling with *Ti*

701   enhancements as representative of frictional heating. This follows the equivalence of the

702   heat exchange term with the frictional heating term as shown in equation 1 [*Thayer and*

703   *Semeter,* 2004]. This brings in the square-law dependence on *Vi* in flow jets and linear

704   dependence on *Ne* ~170-210 km. In darkness, as in this case study, *Ne*(*h*) was enhanced at

705   these altitudes by soft particle fluxes.

706

707   Within the above context we can now proceed to discuss our test of the *Carlson et al*.

708   [2012] mechanism. The advantage of using the field-aligned radar measurements to test the

709   mechanism by measuring *Ti* and *Ne*(*h*) as <u>input</u> to equation (3), was that it required no

710   assumptions about the neutral wind field V_n. Here the rate of change of energy was

711   determined from the relative difference in the ion and neutral thermal energies, i.e. the

712   heat exchange rather than the frictional heating. While *Ne* and *Ti* are the two key measured

713   variables for the ionospheric <u>input</u> in equation (3) of the mechanism we are testing, the

714   narrow field FPI vertical wind is a sensitive measure of the <u>response</u>. We show all three in

715   Figure 6, for the period after the CME during which the cusp was identified from signatures

716   in the radar signal in *Te*, *Ti*, *Ne*, and *Vi* (e.g. *Carlson* [2012] and many references therein), as

717   well as the standard well documented optical signatures of the cusp (e.g. *Sandholt et al*.

718   [2002] and many references therein).   With these conditions in place, we can examine

719   whether this data set of coincident FPI-ESR observations can support or refute the proposed

720   mechanism. While much MSP/ASIP optical and ESR *Ne*, *Te*, *Ti*, *Vi* data exist, as context for

721   whether these observations are representative of common conditions in the cusp, the

722   juxtaposition in time and space of FPI-ESR data is what makes this data set special. Thus, we

723   report here the findings from these observations using time granted by EISCAT for the

724   express purpose of testing the proposed mechanism.

725

726   Figure 7 shows a) electron density (*Ne*), b) narrow field FPI vertical wind (*Uz*), and c) ion

727   temperature (*Ti*), for the three hour period 06:00 – 09:00 UT on 22nd January 2012. The

728   narrow field FPI vertical winds response was extremely clear. The 630 nm intensity was high

729   and so the error bars were on average typically $\pm10\text{ms}^{-1}$ or less. Furthermore, the high time

730   resolution and systematic changes observed in the vertical wind give great confidence to

731   these measurements. The achievement of such precision and reliability of the measurement

732   of such small Doppler shifts produced by vertical winds should be credited to the advent of

733   highly sensitive and fast CCD cameras. *Larsen and Meriwether* [2012] have reviewed the

734   observations of thermospheric vertical winds from all latitudes which show consistent

735   behaviour for observations by different techniques, substantiating the reliability of these

736   observations.

737

738   We focus on the altitude scale 100 to 210 km range identified in the mechanism of *Carlson*

739   *et al.* [2012] as critical to energy injection to the thermosphere. $Ne(h)$ is not only linearly

740   related to energy deposition rate but also serves as an indicative measure of the

741   characteristic energy of the electron particle flux in the ~0.1 -10 keV range, as per ionization

742   production rates in Fig 1f in *Carlson et al.* [2012], and recombination-balanced $Ne(h)$ from

743   the technique developed at the Chatanika Radar [*Wickwar et al*, 1975; *del Pozo et al.*, 1997].

744   Likewise we focus on Ti near 200 km where the heat input has the greatest leverage to drive

745   a strong response in the upper thermosphere.

746

747   After the CME arrived, the cusp expanded equatorward, until overhead, as monitored by

748   auroral intensities observed by SCANDI (Figure 3) and the MSP (data not shown here);

749   Figure 6a shows that the ESR 42 m antenna beam, parallel to the geomagnetic field ($B_{//}$),

750   probed regions of three distinct characters, as illustrated most clearly in the $Ne(h)$ data. The

751   ionosphere much below 200 km has such a short (seconds) chemical lifetime that any

752   plasma seen in the one-minute integration periods in Figure 6a must be produced in-situ.

753   From 06:00 – 07:00 UT, persistent hard particle flux was evidenced by a region of enhanced

754   *Ne* centered near 120 km, well equatorward of the cusp. When closer to the cusp (07:00 –

755   08:00 UT), the hard particle flux became more sporadic with intervals of dominant soft

756   particle precipitation. Shortly after 08:00 UT only soft particle fluxes were seen, confirming

757   the region under the cusp had been reached. Minutes thereafter, the first sign of frictional

758   drag heating was seen, evidenced by the onset of the first significant *Ti* enhancements.

759   During the time 06:00 UT until just before 08:10 UT, *Ti* (possibly excepting one minute)

760   never exceeded 1250 K, which equates to a *Vi* flow jet never reaching 1 kms^{-1} [*St. Maurice*

761   *and Hanson*, 1982].   Thereafter, *Ti* repeatedly exceeded 2000-3000 K, and showed

762   temperatures near 170-200 km reaching momentarily to values as high as 6000K, equating

763   to *Vi* jets up to 3 kms^{-1}. Note that *Ti* was observed to be > 2000 K during the upwelling

764   events, in contrast to < 1250 K between upwelling events. For *Tn* ~1000 K, a *Ti* ~1600 K

765   corresponds to *Vi* ~1000 ms^{-1} and a *Ti* in excess of > 2000 K corresponds to *Vi* in excess of >

766   1300 ms^{-1} [*St Maurice and Hanson*, 1982]. Thus, the observed *Ti* data make absolutely clear

767   that there was significant frictional drag heating present during the upwelling events and

768   absent between upwelling events. The strong thermosphere upwelling events observed

769   corresponded very well with the predictions.

770

771   What we presented in this paper is a collection of measurements that taken together

772   represents a significant test of the new mechanism proposed in [*Carlson et al.*, 2012]. The

773   strong correlation between large values of observed *Ti* (ESR) and *Vn* (FPI) draws attention to

774   higher E-region altitudes, where the thermosphere near 200 km is ~2 orders of magnitude

775   more tenuous. Thus, the cusp (dayside aurora) thermosphere response greatly differs from

776   the energetic-particle dominated night-side auroral thermosphere [*Carlson et al.*, 2006].

777   We should point out in all this that we are not addressing a superstorm or even strong

778   storm conditions [*Liu et al.*, 2011]. The phenomena here can occur commonly provided the

779   IMF was southward facilitating the occurrence of geomagnetic reconnection impacting the

780   cusp.

781

782   *To summarize, the mechanism we test here makes the following predictions:*

783   (1) The thermosphere below ~160 km has too great a heat capacity to respond quickly to

784   any known energy deposition rate. This is demonstrated in Figure 6 which shows the first

785   significant frictional heating event in the cusp at 08:18 UT, when Ti values~2000 K were

786   observed up to an altitude of 170 km. *St Maurice and Hanson* [1982] would attribute such a

787   high ion temperature to a velocity difference ($\underline{V}_i$ - $\underline{V}_n$) ~2000 ms^{-1}. This is supported by the

788   appearance of transient jets seen as CUTLASS line-of-sight speeds > 800 ms^{-1} in Figure 8. Yet

789   no significant FPI upwelling was observed. On close examination two lesser Ti > 1800K

790   heating events can be found at 08:11 and 08:14 UT, both also below 170 km and both also

791   with no evidence of upwelling.   Test not failed.

792   (2) In the altitude region ~160-200 km, the square law dependence of energy deposition

793   rate on plasma speed in the neutral rest frame, or its equivalent Ti dependence, makes the

794   thermosphere highly responsive. This is demonstrated in Figure 6 by the next significant

795   frictional heating event at 08:24 UT, when Ti >2000 K for the first time reached up to 200 km

796   altitude. This was the first time the narrow field FPI showed upwelling, and it did so with the

797   expected time lag of ~2 minutes. Test now passed.

798 (3) Particle precipitation will facilitate upwelling, but the particle flux alone is not sufficient.

799 A *Ti* enhancement is necessary to produce an upwelling, but only if the particle precipitation

800 occurs near the altitude region of 180-210 km. Figure 6 shows significant E region (hard)

801 particle precipitation at 06:16 - 06:21 UT, and 06:35 - 06:49 UT, with several bursts after

802 07:00 UT, and significant lower F region (soft) particle precipitation during 06:22 - 06:34 UT,

803 and 07:15 - 07:20 UT. None of these periods showed *Ti* enhancements and none of these

804 showed upwelling events. However, for altitudes near 180 km all *Ne* enhancements

805 accompanied by *Ti* enhancements did show upwelling events. Furthermore, Figure 8 shows

806 corroboration of large, but transient bursts of line-of-sight ion speeds > 800 ms^{-1} observed

807 by the Hankasalmi radar. Test passed.

808 (4) The response time of the thermosphere above 200 km to these transient events is a few

809 minutes in contrast to ~1-3 hours generally attributed to the lower thermosphere. We have

810 observed response times of minutes, as shown in Figure 6. Test passed.

811

812 We should note other predictions not directly resolved here but either already verified

813 elsewhere or available for others to prove/disprove: (1) The square law dependence leads

814 to significant thermospheric response for *Vi* ~2-3 kms^{-1}. (2) Such high velocities have been

815 observed, and when used in a hydrostatic model, can account for the density/drag

816 doublings seen by *Lühr et al.* [2004] near 400 km altitude over the cusp. (3) Plasma flow jets

817 of 1-2 kms^{-1} occur more frequently in the cusp, which accounts for why density

818 enhancements of only a few tens of percent are more commonly reported by *Lühr et al.*

819 [2004]. Since more than 50% of CHAMP observations show density enhancements > 1.2, it

820 may be possible that *Vi* as small as 500 ms^{-1} may be capable of causing upwelling, though

821   presumably requiring large and opposing *Vi* and *V*n. The assumption of hydrostatic

822   equilibrium in thermospheric models may lead to higher energy requirements than

823   necessary. (4) It is energy deposition near 200 km altitude that matters most. (5) The linear

824   dependence of energy deposition rate on *Ne* means that a few minutes of large *Vi* ~ 2-3

825   kms-^{1} still requires *Ne* > 10^{10} m^{-3} in the region 170-200 km (with significant frictional drag

826   heating turning on around $10^{10.5}$ m^{-3}, becoming quite strong by *Ne* ~10^{11} m^{-3}). (6)

827   Geomagnetic reconnection driven flow jets are common in the cusp but much less common

828   for latitudes beyond two degrees equatorward of the cusp. Note that if the field of view of

829   the ESR is within the region of the reconnection event, the ESR will see enhanced *Ne*

830   simultaneously with the flow jet. However, no enhancement of *Ne* will be observed if the

831   ESR beam is so far downstream that the newly-opened flux tube has already dumped most

832   of the particles available.

833

834   In short, what we observe (most of which is illustrated in Figure 6) is in agreement with all

835   predictions the data can directly either prove or disprove. No upwelling events were seen

836   before 06:00 UT, nor during the first two hours after the arrival of the CME. Once the

837   upwelling events started near 08:25 UT, they continued to occur for the next ~3 hours,

838   during which, the overhead fields of view of the narrow field FPI and ESR were within the

839   expanded active cusp. The first three significant upwelling events after 08:00 UT were

840   relatively distinct events, as seen in Figure 6, and thus, the data were well-suited to the test

841   of these predictions. The six that followed in the next hour (Figure 2c) have not been

842   discussed here since they were so close in time/space that interference among up/down-

843   welling events could have occurred, as was also the situation for the hour following that.

844

845   We regard these details of agreement with predictions as important evidence in support of

846   the proposed mechanism we set out to test. Within the context of other work described in

847   the introduction, *Prolss* [2006] undertook a valuable statistical study of the soft-electron-

848   heating in the cusp, deriving the location and thermal balance of the cusp electron gas.

849   However, otherwise, he did not deal with the densities or thermal balance of the cusp

850   thermosphere, and his study provided a climatological average.   *Crowley et al.* [2010] came

851   closer to realistic modeling of significant thermospheric cusp density enhancements than

852   any prior work. As we suggested in *Carlson et al*.[2012], we attributed this advance largely

853   to the use of data-driven input versus climate-averaged data input to drive the model. The

854   reduced density observed by the Streak satellite from an altitude of ~250 km was used as an

855   argument against frictional heating by *Clemmons et al* [2008]. However, it is consistent with

856   the requirement of the mechanism we are testing here - that the density increase observed

857   near 400 km must come at the expense of a density reduction at altitudes below. The direct

858   impact of soft electron flux energy deposition for thermospheric density enhancement has

859   been found inadequate (only a few percent) to account for the > 20% increase in cusp

860   density regularly observed by CHAMP [e.g. *Sadler et al*., 2012, and *Deng et al*., 2013].

861   *Carlson et al*. [2012] and *Deng et al.* [2013] pointed out that steering the altitudes being

862   heated towards the F region and away from the E region can increase the fractional increase

863   of thermospheric density enhancements from frictional drag/Joule heat input significantly –

864   by 100% and 59% in their respective case studies.

865

866   **4. Conclusions**

867   Simultaneous state-of-the-art observations of the ionosphere by the Svalbard EISCAT Radar

868   and of the thermosphere by both a narrow-field FPI and wide-field SCANDI instruments

869   have shown for the first time that the neutral atmosphere can respond rapidly to cusp

870   frictional-drag heating on the mesoscale, i.e. over a period of tens of minutes or less, with a

871   spatial scale size of a few hundred kilometres. Large, sustained, vertical winds appeared

872   almost immediately provided that the ion frictional drag heating reached a critical threshold

873   (Ti ~2000-2500 K, equivalent to ($\underline{Vi} - \underline{Vn}$) ~ 1.5 km/s), with enhanced electron density in the

874   height region 170-200 km steering the energy deposition from frictional-drag heating to

875   where it had greatest leverage for upwelling. Furthermore, these results show that Joule

876   heating in the E-region did not produce significant upwelling. Although high-speed plasma

877   was required to yield significant upwelling, soft particle precipitation was necessary in the

878   dark cusp for defining the altitude profile of the heat input. This was directly confirmed by

879   our observations. The first two pulses of precipitation seen between 06:17-07:30 UT

880   produced at most a very small systematic upwelling, yet the precipitation that began around

881   08:30 UT was immediately (within ~ 2 minutes) registered by a thermospheric response of a

882   strong resulting upflow. The mechanism proposed by *Carlson et al* [2012] is supported by

883   these observations, where localised heating at high altitudes was easily able to heat and

884   expand the rarefied gas above.

885

886   The possibility of the observations of extreme vertical winds being the consequence of

887   auroral contamination of the narrow field FPI spectra was examined but considered as

888   unlikely. A modeling study of the 630nm emission height profile is planned to investigate

889   the size of the possible contribution by hot oxygen.

890

891   More generally, the principles tested/quantified herein provide observational substance to

892   the suggestion by *Carlson et al.*, [2012] that upper thermosphere densities can rapidly

893   respond at high altitudes with ~tens of percent density enhancements wherever: (1) plasma

894   flow shears ~1000-3000 ms^{-1} make frictional drag energy available for minutes or longer,

895   over only a few hundred kilometers range, and (2) soft particle fluxes steer this energy

896   dissipation to altitudes >~180 km.   We suggest a search for upwelling could prove profitable

897   over the following regions: polar cap arcs [*Ma and Schunk*, 1997], the night-side auroral

898   region where geomagnetic reconnection events can be expected [*Moen et al*, 2007], and

899   regions of large shears such as the Harang discontinuity [*Erickson et al*, 1991].

900

901   Finally, we have demonstrated our mechanism can be modelled using realistic input values

902   in *Carlson et al.* [2012], and is consistent with the observations presented here. We of

903   course can not and do not claim the absence of other mechanisms, especially to account for

904   more moderate density enhancements. For example, *Codrescu et al.* [2000] and *Shepherd*

905   *et al.* [2003] have argued that variability of the electric fields can double the energy input,

906   and there are several mechanisms contributing to production of such variability including

907   fine structure FTE currents [*Oksavik et al.*, 2005] also associated with reconnection event

908   flow shear events. We will next embark on a study to quantify the contribution of this

909   mechanism, with heavy weighting placed on the frequency of occurrence of plasma flow jets

910   exceeding 1500 ms^{-1} in the neutral rest frame, and with particular attention to the terms of

911   the spatial and temporal scales.

912

925

926   **Figure Captions**

927

928   **Figure 1 a)** SCANDI sectors mapped onto a map showing the locations of the IMAGE

929   magnetometers; **b)** IMAGE magnetometers stack plot of x-component. **c)** Latitude-longitude

930   map (in units of kilometers) of the SCANDI field-of-view divided into 61 zones. The top of

931   the figure is geomagnetic north, and the major geographic directions are indicated. The

932   standard look directions of the narrow field FPI are indicated by blue dots; the special NE

933   and SW look directions used for this experiment are indicated by green dots. The ESR field-

934   aligned direction is indicated by a red dot.

935

936   **Figure 2 a)** electron densities along the geomagnetic field line; **b)** narrow field FPI red line

937   intensities; **c)** narrow field FPI vertical and nearly geomagnetic zonal component winds (see

938   text).

939

940   **Figure 3** The SCANDI data for the period 05:57-11:57 UT are shown in three rows. The top

941   (blue) row shows the line-of-sight wind components seen by each of the 61 sectors. The

942   second (green) row shows the neutral temperatures, and the third (red) row shows the 630

943   nm intensities at the peak emission altitude (~240km).

944

945   **Figure 4: a)** Neutral temperatures at the peak emission altitude (~240 km) as measured by

946   the narrow field FPI for 3 look directions and the SCANDI central zone. **b)** 3 hour MSIS model

947   temperatures for the same period showing the values corresponding to the narrow field FPI

948   NE, SW and Zenith volumes. The span distance across the FPI field-of-view is ~800 km

949   diameter. There is a negligible latitudinal gradient in the MSIS temperatures.

950

951   **Figure 5:** SCANDI wind vectors from 61 sectors over the period 05:50-11:57 UT on 22

952   January 2012 ($\chi 2< 16$). The red line indicates the line joining geographic NE and SW, i.e.

953   along the look direction of the narrow field FPI.

954

955 **Figure 6**: 06:00-09:00 UT in 22 January 2012 **a)** electron density 100-210 km; **b)** vertical

956 winds from the narrow field FPI; **c)** ion temperature. No upwelling events were seen for

957 either hard or soft particle precipitation events outside regions of flow-jets, but began

958 immediately upon the first ion frictional-drag ion-heating event (evidenced in *Ti*) near 200

959 km. These heating events recur in the data as long as the active cusp was overhead.

960 Detailed agreement between observations and predictions were taken as strong evidence

961 for the *Carlson et al.* [2012] mechanism tested here.

962

963 **Figure 7:** Examples of transient bursts of large horizontal plasma flow shown by the

964 CUTLASS Hankasalmi radar (part of the SuperDARN radar network) between 0826-0842 UT

965 on 22 Jan 2012 superimposed on a map centred on Svalbard. This was a period of large

966 thermospheric upwelling. A grey circle centred on Svalbard with radius 500km defines the

967 SCANDI field-of-view.

968

969 **Figure 8:** Example of a transient burst of large plasma flow shown by the CUTLASS

970 Hankasalmi and Pykkvibær radars (part of the SuperDARN radar network) within 1 minute of

971 0743 UT on 22 Jan 2012 superimposed on a map centred on Svalbard. A grey circle centred

972 on Svalbard with radius 500km defines the SCANDI field-of-view. Despite the large line-of-

973 sight plasma flows > 800 ms^{-1} seen to the north-east of Svalbard by Hankasalmi and to the

974 south-west by Pykkvibær, there was no upwelling observed at this time by the narrow field

975 FPI.

976

977 **Figure 9:** Frequency of observation statistics from the CUTLASS HF radars of the horizontal

978 components of ion velocities during the period Jan-Dec and 07-11UT (i.e. Svalbard dark

979 cusp) for the years 1997-2009. The data are divided into solar maximum years (1998-2003)

980 in the left hand column, and solar minimum (2005-2009) on the right. The top row shows

981 the Hankasalmi line-of-sight histograms, and the second row the Pykkvibær histograms.

982 Since positive is defined here as positive velocity towards the radar, for this dataset, the

983 Hankasalmi histograms represent the horizontal ion velocity components to the geographic

984 south (V_S) and geographic west (V_W). The third row histograms zoom in on the magnitude of

985 the line-of-sight velocities (blue=Hankasalmi, red=Pykkvibær) to focus on the range 1000-

986 3000 ms^{-1}.

987

988 **References**

989

990 Anderson, B. J., Statistical studies of Pc 3-5 pulsations and their relevance for possible

991 source mechanisms of ULF waves, Ann. Geophysicae, 11, 128–143, 1993.

992 Aruliah, A. L., D. Rees (1995), The Trouble with Thermospheric Vertical Winds: Geomagnetic,

993 Seasonal and Solar Cycle Dependence at High Latitudes, J.Atmos.Terr.Phys, 57, 597-609.

994 Aruliah, A. L., E. M. Griffin, H.-C. I. Yiu, I. McWhirter, and A. Charalambous, (2010), SCANDI –

995 an all-sky Doppler imager for studies of thermospheric spatial structure, Ann. Geophys., 28,

996 549-567.

997 Buneman, O., Excitation of field-aligned sound waves by electron streams, Phys. Rev. Lett.,

998 10, 285-287, 1963.

999   Burns, A. G., T. L. Killeen, and R. G. Roble (1991), A theoretical study of thermospheric

1000   composition perturbations during an impulsive geomagnetic storms, J. Geophys. Res., 96,

1001   14,153–14,167, doi:10.1029/91JA00678.

1002   Carlson, H. C., J. Moen, K. Oksavik, C. Nielsen, I. W. McCrea, T. Pedersen and P. Gallop,

1003   (2006), Direct observations of injection events of subauroral plasma into the polar cap", ,

1004   Geophys. Res. Lett., 33, doi: 10:1029/2005GL025230.

1005   Carlson, H. C., (2012), Sharpening our thinking about polar cap ionospheric patch

1006   morphology, research, and mitigation techniques, Radio Sci., 47, RS0L21,

1007   doi:10.1029/2011RS004946,

1008   Carlson, H. C., T. Spain, A. Aruliah, A. Skjaeveland, and J. Moen (2012), First-principles

1009   physics of cusp/polar cap thermospheric disturbances, Geophys. Res. Lett., 39, L19103,

1010   doi:10.1029/2012GL053034

1011   Clemmons, J. H., J. H. Hecht, D. R. Salem, and D. J. Strickland (2008), Thermospheric density

1012   in the Earth's magnetic cusp as observed by the Streak mission, Geophys. Res. Lett., 35,

1013   L24103, doi:10.1029/2008GL035972.

1014   Codrescu M.V., T.J.Fuller-Rowell, J.C.Foster, J.M.Holt, S.J.Cariglia, (2000), Electric Field

1015   variability associated with the Millstone Hill electric field model, J.Geophys.Res.,105, 5265-

1016   5273.

1017   Conde, M., R. W. Smith, (1998), Spatial structure in the thermospheric horizontal wind

1018   above Poker Flat, Alaska, during solar minimum, J.Geophys.Res., 103, 9449-9471.

1019 Conde, M., J.D.Crave, T.Immel, E.Hoch, H.Stenbaek-Nielson, T.Hallinan, R.W.Smith, J.Olson,

1020 Wei Sun, L.A.Frank, J.Sigwarth, (2001), Assimilated observations of thermospheric winds,

1021 the aurora, and ionospheric currents over Alaska J.Geophys.Res., 106, 10493-10508.

1022 Crowley, G., (1996), A critical review of ionospheric patches and blobs, Review of Radio

1023 Science 1993– 1996, pp. 619– 648, Oxford Univ. Press, New York.

1024 Crowley, G., D. J. Knipp, K. A. Drake, J. Lei, E. Sutton, and H. Lühr (2010), Thermospheric

1025 density enhancements in the dayside cusp region during strong B_Y conditions, Geophys. Res.

1026 Lett., 37, L07110, doi:10.1029/2009GL042143.

1027 Davies, J.A., M.Lester, S.E.Milan, T.K.Yeoman, (1999), A comparison of velocity

1028 measurements from the CUTLASS Finland radar and the EISCAT UHF system, Ann.Geophys.,

1029 17, 892-902.

1030 del Pozo, C.F. and Hargreaves, J.K. and Aylward, A.D. (1997), Ion composition and effective

1031 ion recombination rate in the nighttime auroral lower ionosphere. Journal of Atmospheric

1032 and Solar-Terrestrial Physics, 59 (15). pp. 1919-1943. ISSN 1364-6826

1033 Demars, H. G., R. W. Schunk, (2007), Thermospheric response to ion heating in the dayside

1034 cusp, J. Atmos. Sol. Terr. Phys, 69, 649-660.

1035 Deng, Y., T.J.Fuller-Rowell, A.J.Ridley, D.Knipp, R.E.Lopez, (2013), Theoretical study:

1036 Influence of different energy sources on the cusp neutral density enhancement, 118, 2340-

1037 2349

1038 Dieke, G. H., and D. F. Heath, (1959), The first and second positive bands of N_2, Johns

1039 Hopkins Spectroscopic Report, No. 17.

1040   Drayton, R. A., A. V. Koustov, M. R. Hairston, and J.-P. Villain, Comparison of DMSP cross-

1041   track ion drifts and SuperDARN line-of-sight velocities, Annales Geophysicae, 23, 2479–

1042   2486, 2005

1043   Eliassen, Arnt, (1949), The quasi-static equations of motion with pressure as independent

1044   variable, Geofysiske Publikasjoner, 17 (No. 3), 5-44.

1045   Erickson, G. M.,, R. W. Spiro, R. A. Wolf, The physics of the Harang discontinuity, J. Geophys.

1046   Res., 96, 1633–1645, doi:10.1029/90JA02344.

1047   Etemadi, A., S. W. H. Cowley, M. Lockwood, (1989), The Effect of Rapid Changes in

1048   Ionospheric Flow on Velocity Vectors Deduced From Radar Beam-Swinging Experiments,

1049   J.Atmos.Terr.Phys., 51, 125-138.

1050   Farley, D. T., (1963), A plasma instability resulting in field-aligned irregularities in the

1051   ionosphere, J. Geophys. Res., 63, 6083-6097,

1052   Harris, M. J., N. F. Arnold, and A. D. Aylward (2002), A study into the effect of the diurnal

1053   tide on the structure of the background mesosphere and thermosphere using the new

1054   coupled middle atmosphere and thermosphere (CMAT) general circulation model, Ann.

1055   Geophys., 20, 225–235, doi:10.5194/angeo-20-225-2002.

1056   Hedin, A.E., MSISE model (1990), Planetary and Space Sci., 40, 556, 1992

1057   Kervalishvili, G. N. and H. Lühr, (2013) The relationship of thermospheric density anomaly

1058   with electron temperature, small-scale FAC, and ion up-flow in the cusp region, as observed

1059   by CHAMP and DMSP satellites, Ann. Geophys., 31, 541–554, www.ann-

1060   geophys.net/31/541/2013/doi:10.5194/angeo-31-541-2013

1061   Lühr, H., M. Rother, W. Köhler, P. Ritter, L. Grunwaldt, (2004), Thermospheric up-welling in

1062   the cusp region: Evidence from CHAMP observations, Geophys. Res. Lett., 31, 6, L06805,

1063   10.1029/2003GL019314.

1064   Larsen, M. F., and J. W. Meriwether (2012), Vertical winds in the thermosphere, J. Geophys.

1065   Res., 117, A09319, doi:10.1029/2012JA017843.

1066   Liu, R., Ma, S.-Y., and Lühr, H., (2011), Predicting storm-time thermospheric mass density

1067   variations at CHAMP and GRACE altitudes, Ann. Geophys., 29, 443–453, doi:10.5194/angeo-

1068   29-443-2011.

1069   Link, R., and L. L. Cogger (1988), A re-examination of the OI 6300-Å nightglow, J. Geophys.

1070   Res., 93, 9883–9892, doi:10.1029/JA093iA09p09883.

1071   Ma, T. Z., and R. W. Schunk (1997), Effect of sun-aligned arcs on the polar thermosphere, J.

1072   Geophys. Res., 102, 9729–9735.

1073   Milan, S. E., T. K. Yeoman, M. Lester, E. C. Thomas, T. B. Jones, (1997) Initial backscatter

1074   occurrence statistics from the CUTLASS HF radars, Ann. Geophysicae 15, 703-718.

1075   Milan, S. E., J. A. Davies, M. Lester, (1999), Coherent HF radar backscatter characteristics

1076   associated with auroral forms identified by incoherent radar techniques: A comparison of

1077   CUTLASS and EISCAT observations, J. Geophys. Res., 104, 22,591-22,604.

1078   Milan, S. E., M.Lester, N.Sato, Multi-frequency observations of E-region HF radar aurora,

1079   (2003), Annales Geophysicae, 21, 761–777.

1080   Moen, J., N. Gulbrandsen, D. A. Lorentzen and H.C. Carlson (200), On the MLT distribution of

1081   F region polar cap patches at night, Geophys. Res. Lett., 34, L14113,

1082   doi:10.1029/2007GL029632.

1083 Oksavik, K., J. Moen and H.C. Carlson, R. A. Greenwald, S. E. Milan, M. Lester, W. F. Denig,

1084 and R. J. Barnes, Multi-instrument mapping of the small-scale flow dynamics related to a

1085 cusp auroral transient,(2005), Ann. Geophys., 23, 2657-2670.

1086 Prölss, G. W. (2006), Electron temperature enhancement beneath the magnetospheric cusp,

1087 J. Geophys. Res., 111, A07304, doi:10.1029/2006JA011618.

1088 Picone, J.M., Hedin, A.E., Drob, D.P., Aikin, A.C., (2002) NRLMSISE-00 empirical model of the

1089 atmosphere: Statistical comparisons and scientific issues, J.Geophys.Res. 107, A12, 1468,

1090 Price, G. D., R.W. Smith, and G. Hernandez, (1995), Simultaneous measurements of large

1091 vertical winds in the upper and lower thermosphere, J. Atmos.Terr. Phys., **57**, 631–643.

1092 Rinne, Y., J. Moen, K. Oksavik, and H. C. Carlson (2007), Reversed flow events in the winter

1093 cusp ionosphere observed by the European Incoherent Scatter (EISCAT) Svalbard radar, J.

1094 Geophys. Res., 112, A10313, doi:10.1029/2007JA012366.

1095 Robinson, R. M., R. R. Vondrak, K. Miller, T. Dabbs, and D. Hardy (1987), On calculating

1096 ionospheric conductances from the flux and energy of precipitating electrons, J. Geophys.

1097 Res., 92(A3), 2565–2569, doi:10.1029/JA092iA03p02565.

1098 Sadler, F.B., M. Lessard, E. Lund, A. Otto, H. Lühr, (2012), Auroral precipitation/ion upwelling

1099 as a driver of neutral density enhancement in the cusp, JASTP, 87-88, 82-90.

1100 Sandholt,P.E., W.F.Denig, C.J. Farrugia, B. Lybekk, E. Trondsen, (2002), Auroral structure at

1101 the cusp equatorward boundary: Relationship with the electron edge of low-latitude

1102 boundary layer precipitation, Journal of Geophysical Research, Volume 107, Issue A9, pp.

1103 SMP 10-1, CiteID 1235, DOI 10.1029/2001JA005081.

1104   Schunk, R. W., and A. Nagy (2009), Ionospheres: Physics, Plasma Physics, and Chemistry, 2nd

1105   ed., Cambridge Univ. Press, New York, doi:10.1017/ CBO9780511635342

1106   Shematovich, V.I., D.V.Bisikalo, J.-C.Gerard, (1994), A kinetic model of the formation of the

1107   hot oxygen geocorona, 1. Quiet magnetic conditions, J.Geophys.Res, 100, 3715-3720.

1108   Shepherd, S.G., J.M.Ruohoniemi, R.A.Greenwald, (2003), Direct measurements of the

1109   ionospheric   convection   variability   near   the   cusp/throat,   GRL,   30,   2109,

1110   doi:10.1029/2003GL017668.

1111   St. Maurice, J-P. and W. B. Hanson, (1982), Ion frictional heating at high latitudes and its

1112   possible use for an in situ determination of neutral thermospheric winds and temperatures,

1113   J. Geophys. Res., 87, 7580-7602.

1114   Thayer, J. P., and J. Semeter, (2004), The convergence of magnetospheric energy flux in the

1115   polar atmosphere, J. Atmos. Solar-Terr. Phys., 66, 807-824.

1116   Vlasov, M. N., M. J. Nicolls, M. C. Kelley, S. M. Smith, N. Aponte, and S. A. González (2005),

1117   Modeling of airglow and ionospheric parameters at Arecibo during quiet and disturbed

1118   periods in October 2002, J.Geophys. Res., 110, A07303, doi:10.1029/2005JA011074.

1119   Wickwar, V. B., M. J. Baron, R. D. Sears, (1975), Auroral energy input from energetic

1120   electrons and Joule heating at Chatanika, J. Geophys. Res., 80, 4364-4367, 1975.

1121   Zhang, B., W. Lotko, O. Brambles, M. Wiltberger, W. Wang, P. Schmitt, and J. Lyon (2012),

1122   Enhancement of thermospheric mass density by soft electron precipitation, Geophys. Res.

1123   Lett., 39, L20102, doi:10.1029/2012GL053519.

1124
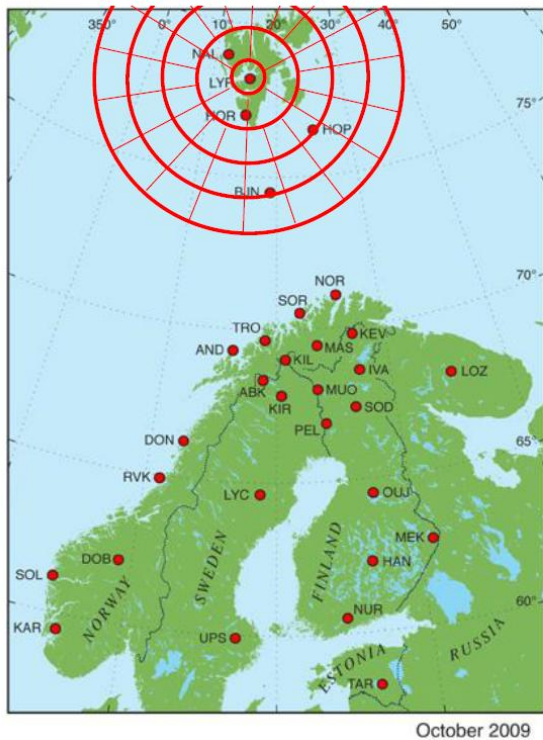
1125

1126   **Figure 1 a)** SCANDI sectors mapped onto a map showing the locations of the IMAGE

1127   magnetometers; **b)** IMAGE magnetometers stack plot of x-component. **c)** Latitude-longitude

1128   map (in units of kilometers) of the SCANDI field-of-view divided into 61 zones. The top of

1129   the figure is geomagnetic north, and the major geographic directions are indicated. The

1130   standard look directions of the narrow field FPI are indicated by blue dots; the special NE

1131   and SW look directions used for this experiment are indicated by green dots. The ESR field-

1132   aligned direction is indicated by a red dot.

1133

1134
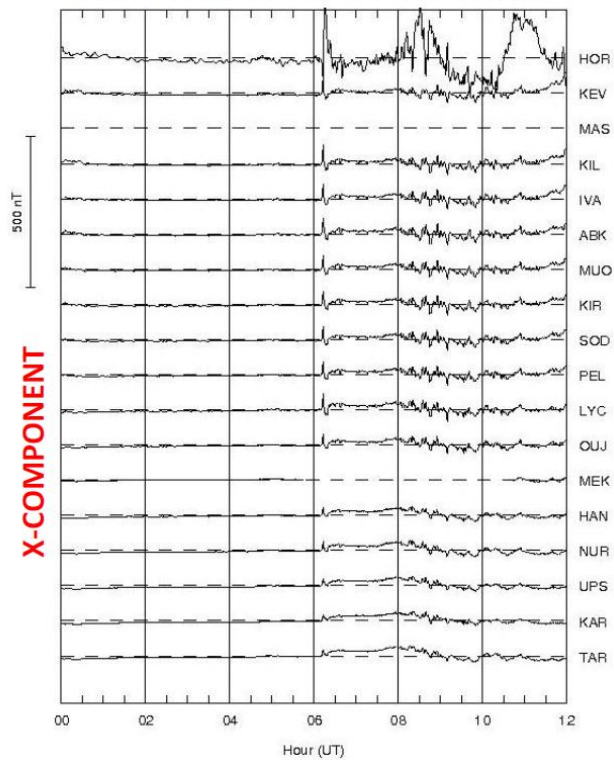
Figure 1 c) Latitude-longitude map (in units of kilometers) of the SCANDI field-of-view divided into 61 zones. The top of the figure is geomagnetic north, and the major geographic directions are indicated. The standard look directions of the narrow field FPI are indicated by blue dots; the special NE and SW look directions used for this experiment are indicated by green dots. The ESR field-aligned direction is indicated by a red dot.
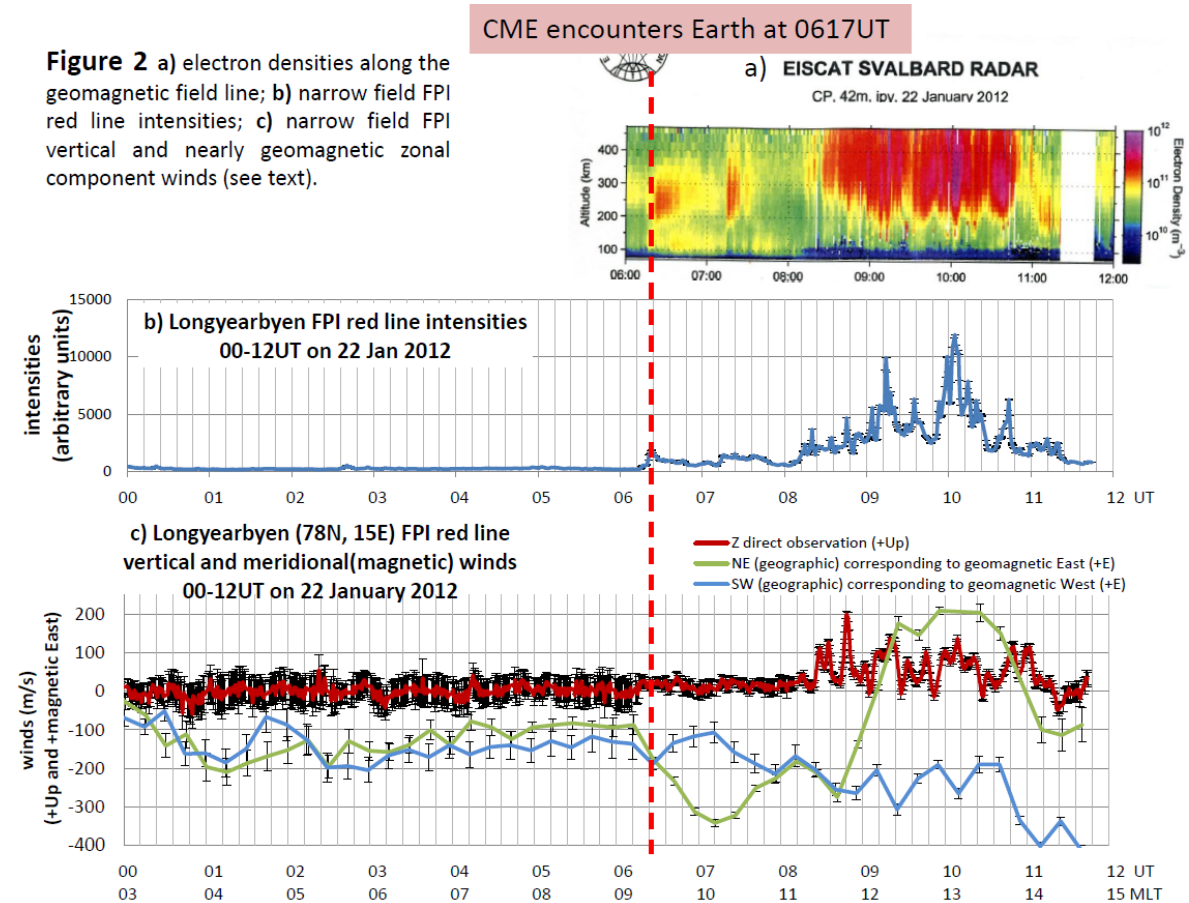
Figure 2 a) electron densities along the geomagnetic field line; **b)** narrow field FPI red line intensities; **c)** narrow field FPI vertical and nearly geomagnetic zonal component winds (see text).

1142

1143   **Figure 2 a)** electron densities along the geomagnetic field line; **b)** narrow field FPI red line

1144   intensities; **c)** narrow field FPI vertical and nearly geomagnetic zonal component winds (see

1145   text).

1146

1147
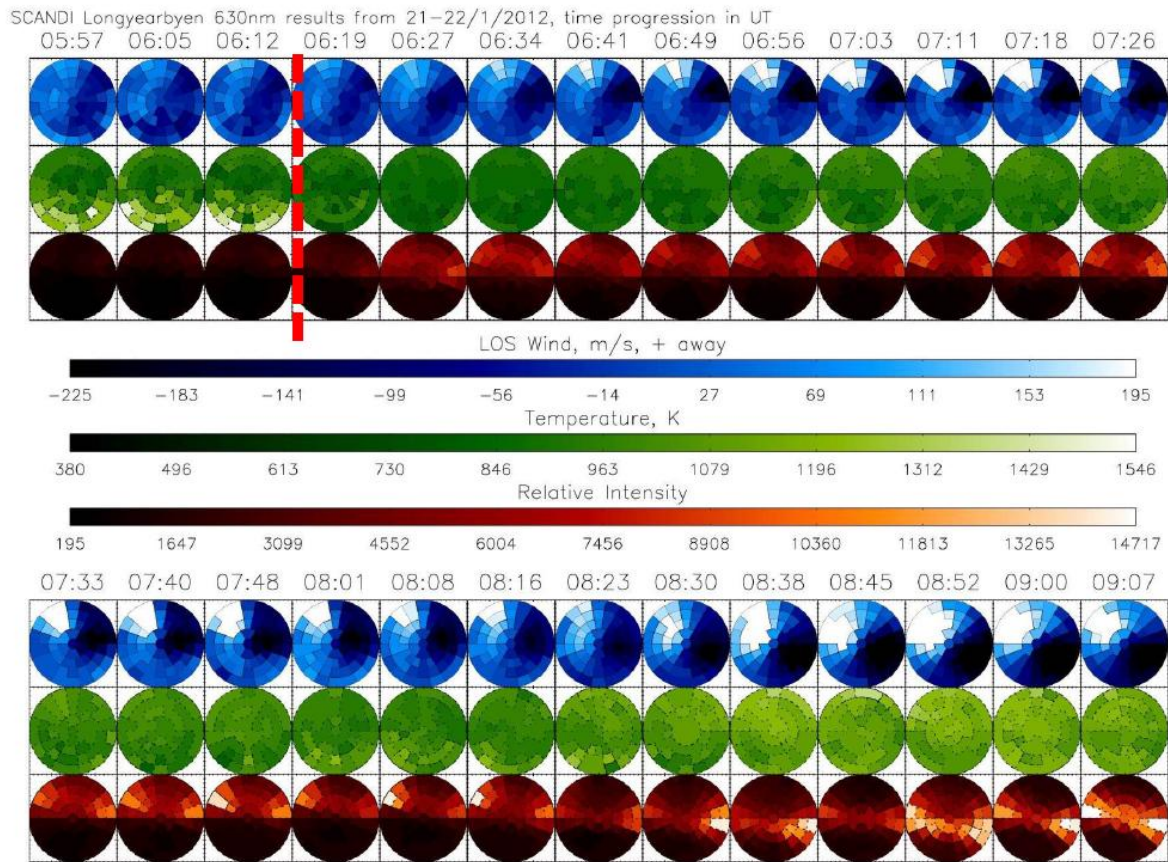
Figure 3 The SCANDI data for the period 05:57-11:57 UT are shown in three rows. The top (blue) row shows the line-of-sight wind components seen by each of the 61 sectors. The second (green) row shows the neutral temperatures, and the third (red) row shows the 630 nm intensities at the peak emission altitude (~240km).

1154
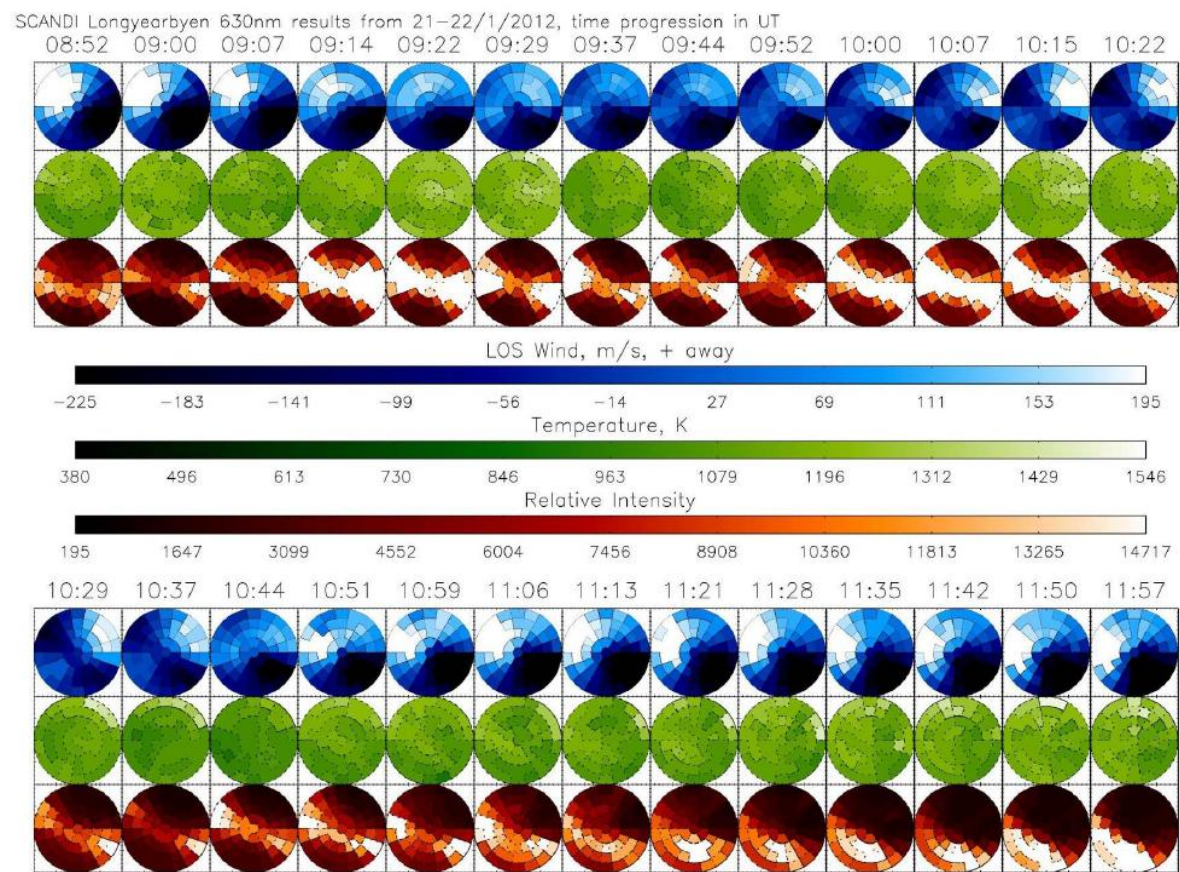
Figure 3 continued, using same scaling.
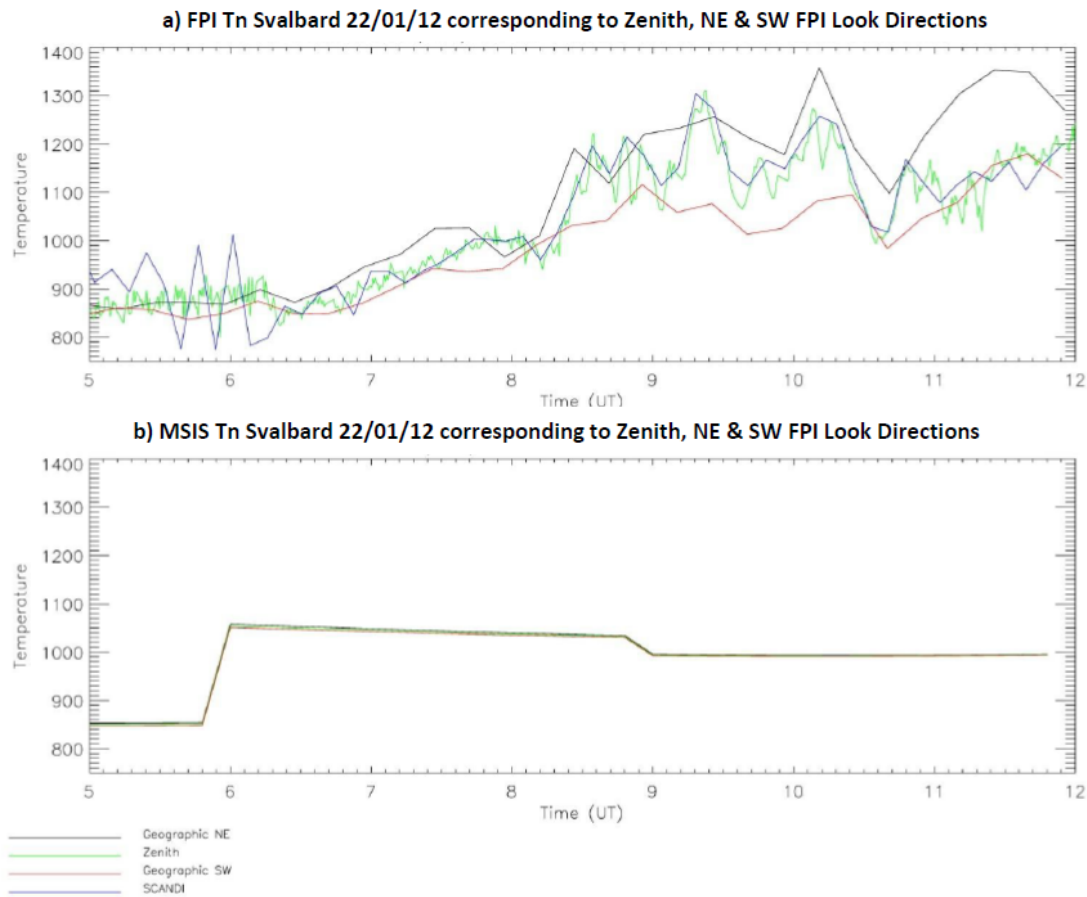
1155

1156

1157

1158

1159

1160

1161

1162

1163 **Figure 4: a)** Neutral temperatures at the peak emission altitude (~240 km) as measured by

1164 the narrow field FPI for 3 look directions and the SCANDI central zone. **b)** 3 hour MSIS model

1165 temperatures for the same period showing the values corresponding to the narrow field FPI

1166 NE, SW and Zenith volumes. The span distance across the FPI field-of-view is ~800 km

1167 diameter. There is a negligible latitudinal gradient in the MSIS temperatures.

1168

1169
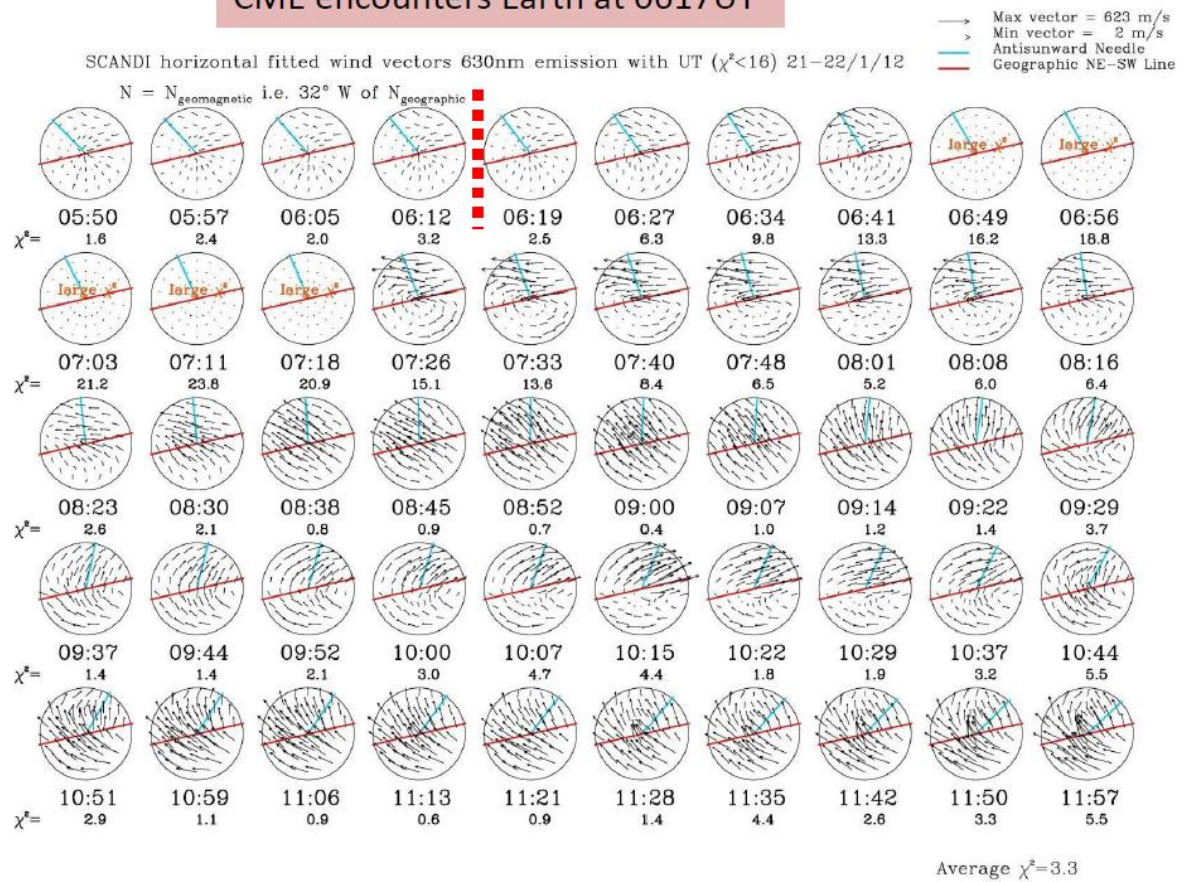
1170

1171 **Figure 5:** SCANDI wind vectors from 61 sectors over the period 05:50-11:57 UT on 22

1172 January 2012 ($\chi 2 < 16$). The red line indicates the line joining geographic NE and SW, i.e.

1173 along the look direction of the narrow field FPI.

1174

1175

1176
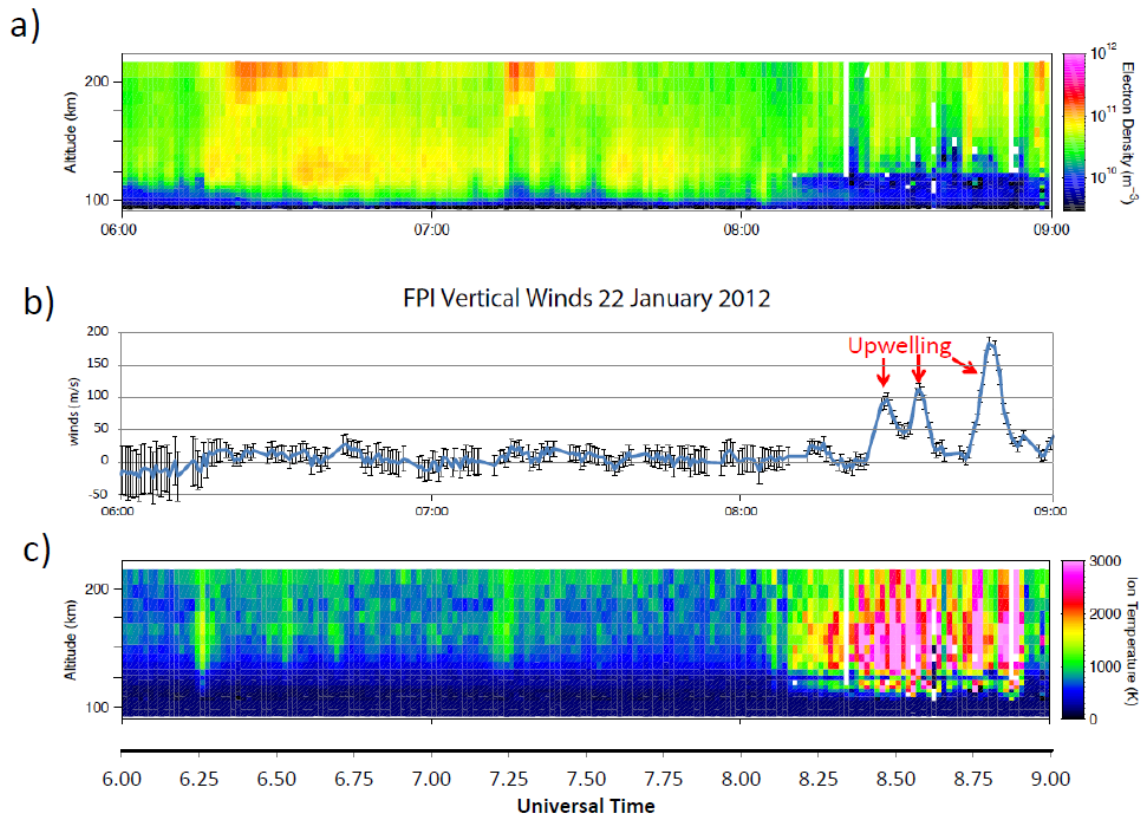
Figure 6: 06:00-09:00 UT in 22 January 2012 **a)** electron density 100-210 km; **b)** vertical

winds from the narrow field FPI; **c)** ion temperature. No upwelling events were seen for

either hard or soft particle precipitation events outside regions of flow-jets, but began

immediately upon the first ion frictional-drag ion-heating event (evidenced in *Ti*) near 200

km. These heating events recur in the data as long as the active cusp was overhead.

Detailed agreement between observations and predictions were taken as strong evidence

for the *Carlson et al.* [2012] mechanism tested here.
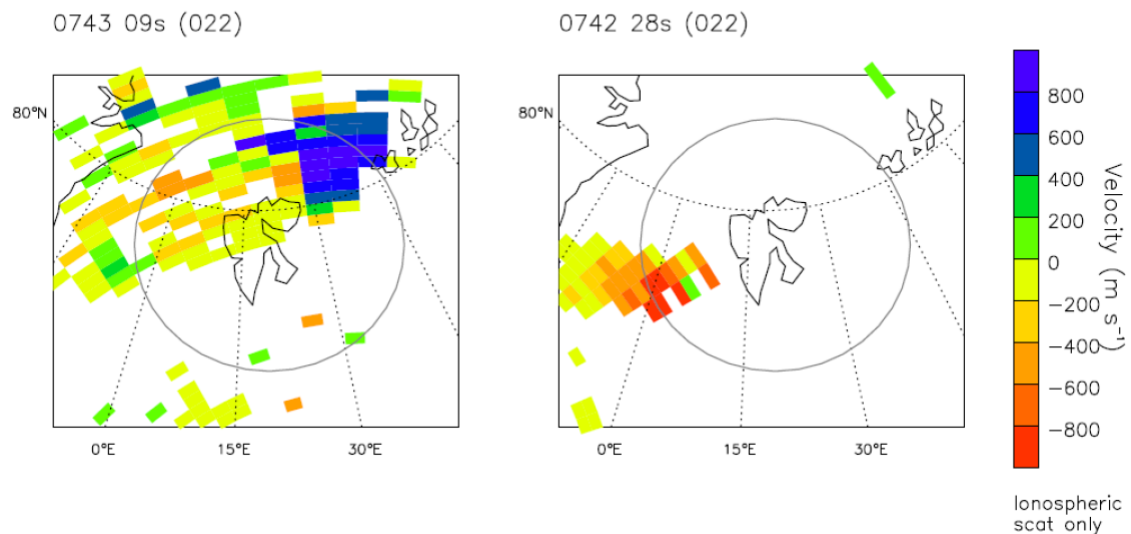
1186

1187 **Figure 7:**   Examples of transient bursts of large horizontal plasma flow shown by the

1188 CUTLASS Hankasalmi radar (part of the SuperDARN radar network) between 0826-0842 UT

1189 on 22 Jan 2012 superimposed on a map centred on Svalbard. This was a period of large

1190 thermospheric upwelling. A grey circle centred on Svalbard with radius 500km defines the
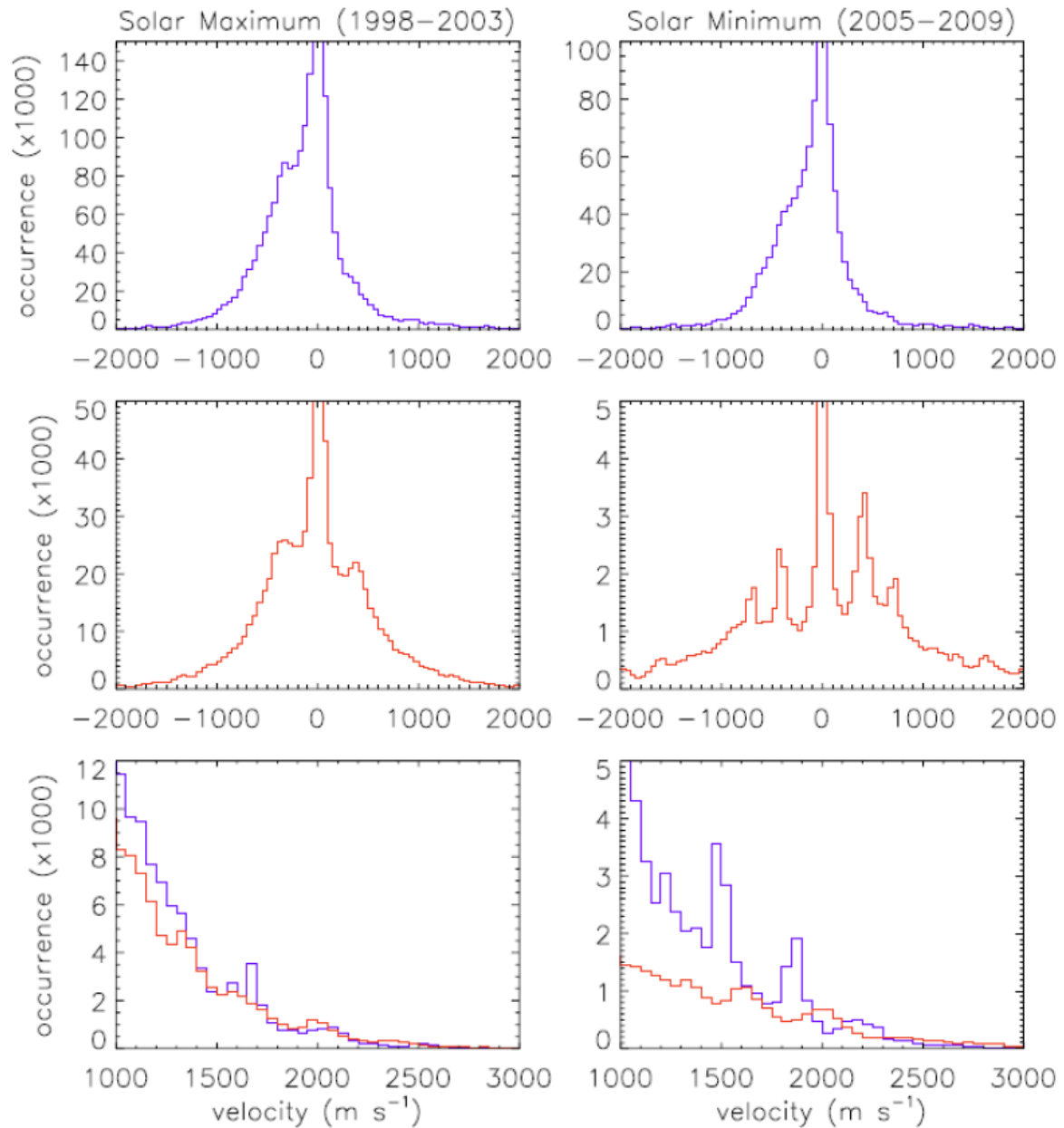
1191 SCANDI field-of-view.

1192

1193

1194

1195
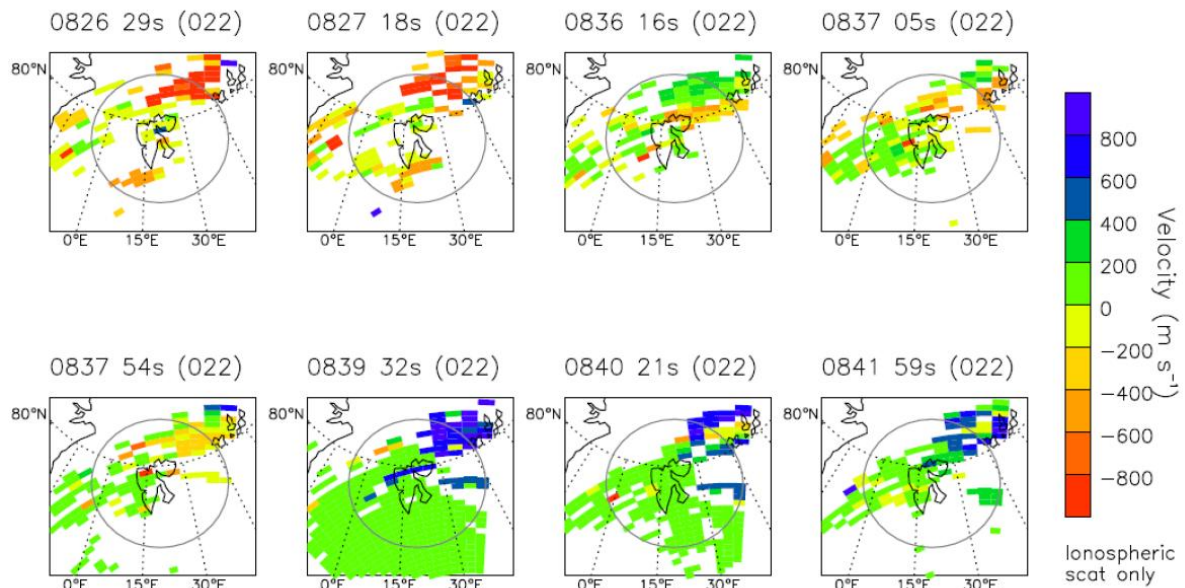
Figure 8: Example of a transient burst of large plasma flow shown by the CUTLASS Hankasalmi and Pykkvibær radars (part of the SuperDARN radar network) within 1 minute of 0743 UT on 22 Jan 2012 superimposed on a map centred on Svalbard. A grey circle centred on Svalbard with radius 500km defines the SCANDI field-of-view. Despite the large line-of-sight plasma flows > 800 ms^{-1} seen to the north-east of Svalbard by Hankasalmi and to the south-west by Pykkvibær, there was no upwelling observed at this time by the narrow field FPI.

1208

Figure 9: Frequency of observation statistics from the CUTLASS HF radars of the horizontal

components of ion velocities during the period Jan-Dec and 07-11UT (i.e. Svalbard dark

cusp) for the years 1997-2009. The data are divided into solar maximum years (1998-2003)

in the left hand column, and solar minimum (2005-2009) on the right. The top row shows

the Hankasalmi line-of-sight histograms, and the second row the Pykkvibær histograms.

Since positive is defined here as positive velocity towards the radar, for this dataset, the

1215   Hankasalmi histograms represent the horizontal ion velocity components to the geographic

1216   south (V_S) and geographic west (V_W). The third row histograms zoom in on the magnitude of

1217   the line-of-sight velocities (blue=Hankasalmi, red=Pykkvibær) to focus on the range 1000-

1218   3000 ms^{-1}.

1219